Applicability of LaNiO$_3$-derived catalysts as dual function materials for CO$_2$ capture and in-situ conversion to methane

Jon A. Onrubia-Calvo , Alejandro Bermejo-López , Sonia Pérez-Vázquez , Beñat Pereda-Ayo , José A. González-Marcos , Juan R. González-Velasco [*]

Department of Chemical Engineering, Faculty of Science and Technology, University of the Basque Country UPV/EHU, Campus de Leioa, Barrio Sarriena, ES-48940 Leioa, Bizkaia, Spain

A B S T R A C T

The valorisation of CO$_2$ through its capture and in-situ hydrogenation to methane, using dual function materials (DFMs), emerges as promising alternative to reduce CO$_2$ emissions to atmosphere and the global cost of current CO$_2$ Capture and Utilization (CCU) technology. This work investigates the viability of LaNiO$_3$-derived formulations as precursors of DFMs for CO$_2$ capture and in-situ conversion to CH$_4$. For this purpose, a set of DFMs obtained from 30% LaNiO$_3$/CeO$_2$, 30% LaNiO$_3$/Al$_2$O$_3$, 30% LaNiO$_3$/La-Al$_2$O$_3$ and LaNiO$_3$ precursors were synthesized and systematically characterized before and after a controlled reduction process. Results of XRD analysis, STEM-EDX images, H$_2$-TPR and CO$_2$-TPD experiments reveal that the DFM obtained after reduction of 30% LaNiO$_3$/CeO$_2$ formulation shows the smallest Ni^0 particle size (7 nm) and the highest medium-strong basic sites concentration. In fact, this DFM widens operation window with methane production ranging between 80 and 103 μmol g^{-1} and maintains a selectivity towards methane above 90% in the range of 280–520 °C. The best catalytic behaviour is related to a better contact between the different nature basic sites and the homogenously distributed Ni^0 sites, which favours a fast spill-over of dissociated H to near CO$_2$ adsorption sites. The applicability of this formulation is further evidenced by a highly stable CH$_4$ production during long-term experiments and a promoted Ni^0/NiO reversibility in the absence/presence of O$_2$ during the CO$_2$ adsorption period, which allows a fast and complete recovery of CH$_4$ production in absence of O$_2$. These aspects favour a versatile application of the 30% LaNiO$_3$/CeO$_2$-based DFM formulation to convert CO$_2$ outlet streams from combustion flue gases of different nature.

1. Introduction

The increase in global energy demand has led to a rapid growth in the fossil fuels consumption. As a result, the emission of greenhouse gases has been constantly increasing during the last decades, contributing to global warming and ultimately to climate change [1]. CO$_2$, mainly emitted from the power generation sector and the industrial and transportation vehicles, is a major contributor to global warming due to its huge emission amounts [2,3]. Thus, the reduction of the CO$_2$ emissions to the atmosphere is essential to limit global warming. In this context, carbon capture and sequestration (CCS) from industry and energy related sources as well as the increase in the efficiency of industrial processes and the widespread implementation of renewable energies, are expected to play an important role in overcoming this increasing problem [4]. However, CCS technology requires captured CO$_2$

purification and transport to storage places and its isolation, which increases drastically the cost and the energy consumption of the process [5,6].

During the last years, there is keen interest in the integration of CO$_2$ capture and its utilization (ICCU), since this technological alternative allows reducing the cost of the overall process by eliminating transportation and storage of CO$_2$ by its conversion to fuels or value-added chemicals [7]. Farrauto et al. [8,9] have patented in 2015 the use of dual function materials (DFMs) to convert the captured CO$_2$ from diluted exhaust gases into methane in a single reactor. Such ICCU process can be even greener when is carried out with hydrogen obtained by the electrolysis of water using surplus renewable energies, contributing at the same time to store excess electrical energy in the form of methane. Therefore, ICCU-methanation technology reduces CO$_2$ emissions to the atmosphere and contributes to solve the problem of intrinsic intermittency of renewable sources [10]. Moreover, the cycling operation, in

Nomenclature

CB	Carbon Balance (%)
F_i^{in}	Molar flow at the reactor inlet of the component i (μmol min^{-1})
F_i^{out}	Molar flow at the reactor outlet of the component i (μmol min^{-1})
S_{CH_4}	Selectivity towards CH$_4$ (%)
STO_{CO_2}	CO$_2$ stored (μmol g^{-1})
t	Time (min)
T	Temperature (°C)
W	Sample mass (g)
Y_{CH_4}	CH$_4$ production (μmol g^{-1})
Y_{CO}	CO production (μmol g^{-1})
Y_{H_2O}	H$_2$O production (μmol g^{-1})

Acronyms

CCS	CO$_2$ Capture and Sequestration
CCU	CO$_2$ Capture and Utilization
DFM	Dual Function Material
EDS	Energy Dispersive Spectroscopy
ICCU	Integration of CO$_2$ Capture and Utilization
ICP-AES	Inductively Coupled Plasma Atomic Emission Spectroscopy
LNO	LaNiO$_3$ perovskite
NP	Nanoparticles
SNG	Synthetic Natural Gas
STEM-HAADF	Scanning Transmission Electron Microscopy - High Angle Annular Dark Field
TCD	Thermal Conductivity Detector
TPD	Temperature Programmed Desorption
TPR	Temperature Programmed Reduction
XRD	X-Ray Diffraction

contrast to the observed for the continuous hydrogenation of CO$_2$, can be directly applied to an effluent gas without the necessity of additional heat input to perform the CO$_2$ capture and does not need purification steps, which reduces the global costs of the process [11].

The selected DFM should selectively capture CO$_2$ from steam- and O$_2$-containing flue gas at different temperatures (200–550 °C), depending on the application and effluent gas properties; and then hydrogenate the adsorbed species to methane with H$_2$ in a carbon neutral cycle. The overall CO$_2$ adsorption-hydrogenation process follows the stoichiometry of the Sabatier reaction [12], which is thermodynamically favoured at low temperature due to its strong exothermicity.

$$CO_2 + 4H_2 \rightleftarrows CH_4 + 2H_2O \quad \Delta H^0 = -164\,kJ\,mol^{-1} \quad (1)$$
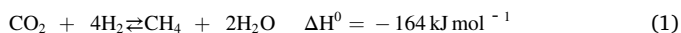
However, the stable electronic structure of the CO$_2$ molecule makes its activation difficult under mild conditions, such as low temperature and low pressure. The use of high reaction temperatures favours the kinetics of CO$_2$ to CH$_4$ conversion; however, it contributes to increase the equipment investment as well as the operational cost, which is undesirable for large-scale industrial utilization. Therefore, a high-performance catalyst that can activate CO$_2$ and promote the reaction rate under relative low temperatures and pressures is vital for its widespread implementation. Based on the characteristics of dual operation, these catalysts require the presence of a storage material for CO$_2$ capture and an active site for H$_2$ activation and CO$_2$ hydrogenation to methane. Regarding to the CO$_2$ adsorption functionality in DFMs, a wide variety of alkali/alkaline-earth phases have been proposed as CO$_2$ storage material, mainly Na [13,14], Ca [8,15], Mg [4,16] or K [4,17]. These storage components should be capable to reversibly operate at intermediates-high temperatures (200–450 °C) [18]. On the other hand, the catalytic and hydrogenation sites are usually based on Ni [15,19–21], Ru [13,14,22,23] or Rh [24] metals. Among them, Ni presents the best cost to activity ratio, which makes this alternative most suitable for industrial applications. Finally, both phases are usually dispersed on a high surface area carrier in order to increase the methane production. In this sense, previous studies reported that γ-Al$_2$O$_3$ is the most appropriate support among other materials [19,25].

Ni-based catalysts prepared by conventional preparation methods often lead to large and heterogeneous particle size distribution, which limits the control over the interaction between the metal nanoparticles (NPs) and the support [26]. Hence, Ni-based catalysts present limited catalytic activity at low temperatures and can be easily deactivated due to the metal sintering occurring at high temperatures. Furthermore, Ni-based DFMs have been considered only for process at intermediate-high temperatures, since Ni can be readily oxidized during the CO$_2$

adsorption period but not easily reduced back during the hydrogenation step at low temperatures [11,19]. Intense efforts have been made in order to design and improve Ni-based catalysts for their application as dual function materials (DFMs). The catalytic behaviour of the Ni-based materials depends on several factors such as the type of support, Ni loading, addition of a second metal and preparation method [27,28,29].

Largely based on the pioneering research of Daihatsu and Toyota, the ex-solution of active metal NPs from an oxide host, such as perovskite-type lattice, has been identified as a simple way to achieve a homogeneous active sites distribution, with good reversibility and controlled interactions between metal and the support [30]. This concept has been already explored for controlling Ni particle sizes and distribution of the catalysts used in the stationary CO$_2$ methanation process [31–33]. Specifically, LaNiO$_3$-type perovskites, partially doped with different components (i.e., Ce, K or Ca), have been proposed as promising host materials to carry out the inside-outside ex-solution of Ni NPs. Nevertheless, non-supported perovskites exhibited rather low surface areas, which could limit the active sites dispersion and the reaction intermediates diffusion. To address the aforementioned limitations, Li et al. [34] and Wang et al. [35] distributed LaNiO$_3$-type perovskites on silica supports. The obtained catalysts have shown improved CO$_2$ methanation efficiency. Based on the well-known promoting effect observed for ceria in its application to the conventional Ni/CeO$_2$ catalyst for the stationary CO$_2$ methanation [36–38], we recently explored the viability of ceria-supported LaNiO$_3$ perovskites as precursor of highly active and stable materials for the continuous CO$_2$ methanation [39]. These catalysts present notably higher methane production than the conventional Ni/CeO$_2$ catalyst and that obtained from the bulk LaNiO$_3$ in the stationary CO$_2$ to CH$_4$ hydrogenation process. Nevertheless, to the best of the authors' knowledge, the use of LaNiO$_3$ perovskite as precursor of highly efficient DFM material for CO$_2$ capture and hydrogenation to methane has not been published to date.

Considering this background, the aim of this work is to evaluate for the first time in the scientific literature the applicability of supported LaNiO$_3$ perovskites, as precursors of efficient dual function materials for CO$_2$ adsorption and in-situ hydrogenation to methane. For that, the previously developed 30% LaNiO$_3$/CeO$_2$ formulation as well as others here synthesized over conventional DFM supports, such as Al$_2$O$_3$ and La-Al$_2$O$_3$, are evaluated in cycles of CO$_2$ adsorption and hydrogenation to CH$_4$. Taking into account the characterization results, the interrelationships between physico-chemical properties, activity, and stability are discovered.

2. Experimental

2.1. Perovskite-based formulations preparation

Prior to the preparation of perovskite-based formulations, different supports were obtained. On the one hand, the ceria support was obtained by direct calcination of the Ce(NO$_3$)$_3$·6H$_2$O (*Sigma Aldrich,* 99.9%) precursor at 500 °C for 4 h in static air. On the other hand, the 5 wt% La-Al$_2$O$_3$ support was obtained by wetness impregnation method over previously calcined γ-Al$_2$O$_3$ (650 °C, 2 h). For that, the amount of La(NO$_3$)$_2$·6H$_2$O (*Merck,* 99.0%), neccesary to obtain a 5 wt% of La$_2$O$_3$ over the support, was incorporated onto γ-Al$_2$O$_3$ (*Saint Gobain*, SA6173) inside a rotary evaporator (vacuum and 35 °C).

Once different supports (Al$_2$O$_3$, La-Al$_2$O$_3$ and CeO$_2$) were obtained, supported perovskites were prepared by combining citric acid and impregnation methods, as reported elsewhere [39]. For that, nominal perovskite loading of 30 wt% was impregnated over these supports. The adopted nomenclature for the fully formulated samples was the following: LNO, 30% LNO/CeO$_2$, 30% LNO/Al$_2$O$_3$ and 30% LNO/La-Al$_2$O$_3$. Note that this nomenclature corresponds to the precursors of the catalysts for CO$_2$ methanation reaction. In order to obtain different DFMs, these precursors were in-situ reduced in the reaction bench.

2.2. Catalysts characterization

X-ray diffraction (XRD) analyses of the fresh and used samples were carried out using a *Philips PW1710* diffractometer. For that, all samples were subjected to Cu K$_\alpha$ radiation in a continuous scan mode in the 2θ range 5–70° with 0.02° per second sampling interval. PANalytical X'pert HighScore and *Winplotr* profile fitting software were used for data treatment. ICDD (International Centre for Diffraction Data) database cards were used for comparative purposes to identify the phases present in the samples.

Scanning Transmission Electron Microscopy - High Angle Annular Dark Field (STEM-HAADF) images were taken for the samples after reduction and CO$_2$ methanation reaction with a Cs-image-corrected Titan (Thermofisher Scientific). This equipment operated at a working voltage of 300 kV, and was equipped with a CCD camera (Gatan) and a HAADF detector (Fischione). The instrument has a normal field emission gun (Shottky emitter) equipped with a SuperTwin lens. Alternatively, the TEM apparatus was also equipped for X-ray Energy Dispersive Spectroscopy (EDS) experiments with an Ultim Max detector (Oxford Instruments). A 2 k × 2 k Ultrascan CCD camera (Gatan) was positioned before the filter for TEM imaging, using an energy resolution of 0.7 eV. The acquisition time for the analysis was 50 ms per spectrum and the used energy dispersion was 0.2 eV pixel^{-1}. Prior to these experiments, the samples were sonicated in ethanol and dropped onto a holey, amorphous carbon film supported on a copper grid.

Textural properties of the fresh and used samples, that is, after controlled reduction and CO$_2$ methanation, were determined by N$_2$ adsorption–desorption isotherms at −196 °C, using a *Micromeritics TRISTAR II* equipment. All samples were pretreated with flowing N$_2$ on a *Micromeritics SmartPrep* instrument at 300 °C for 10 h.

La, Ni, Al and Ce contents were quantitatively determined by Inductively Coupled Plasma Atomic Emission Spectroscopy (ICP–AES). The analyses were carried out using a mass spectrometer with a plasma source (*Q-ICP-MS XSeries II* model of Thermospectrometer). Prior to the analysis, the samples were digested at 120 °C with an acid mixture (HNO$_3$:HCl = 1:3) inside a microwave furnace.

The redox behaviour of the fresh samples was examined by means of Temperature Programmed Reduction with a 5% H$_2$/Ar mixture (H$_2$-TPR) in a *Micromeritics AutoChem II* equipment. For that, the quartz tube reactor was loaded with 0.1 g of sample, which was pretreated in 30 mL min^{-1} of 5% O$_2$/He mixture at 600 °C for 30 min. Then, the sample was cooled down to 35 °C under inert conditions, and finally the temperature was increased from 35 to 950 °C in a 5% H$_2$/Ar mixture (30 mL min^{-1})

using a heating rate of 10 °C min^{-1}. Water generated during samples reduction was removed by condensation in a cold trap placed before TCD detector. The outlet gas stream was continuously monitored with a *Hiden Analitical HPR-20 EGA* mass spectrometer.

The basicity of the samples was evaluated by Temperature Programmed Desorption of CO$_2$ (CO$_2$-TPD) experiments, which were carried out in a *Micromeritics AutoChem II* equipment. The quartz tube reactor was loaded with 0.15 g of the fresh samples. Aiming to obtain a catalytic material similar to that analyzed in the activity test, bulk perovskite and ceria- and alumina-supported samples were completely reduced in a 5% H$_2$/Ar mixture (50 mL min^{-1}) at 650, 550 or 800 °C (2 h), respectively. Then, the reduced samples were cooled down to 40 °C, under inert conditions (He flow stream). Once this temperature was reached, the adsorption of CO$_2$ was performed by exposing the samples to a 5% CO$_2$/He flow stream (50 mL min^{-1}) for 60 min. Finally, the samples were heated from 40 to 900 °C at 10C min^{-1} in He (50 mL min^1) and the desorbed gases were continuously monitored with a *Hiden Analitical HPR-20 EGA* mass spectrometer.

2.3. Catalytic activity

CO$_2$ adsorption and hydrogenation cycles were carried out in a vertical stainless steel tubular reactor inside a 3-zone tube furnace. The reactor was filled with 1.0 g of pelletized (0.3–0.5 mm) fresh formulation, where the operating temperature was continuously measured through a thermocouple placed in the centre of the catalytic bed. Prior to the catalytic test, fresh samples were in-situ reduced with a stream composed of 10% H$_2$/Ar leading to the conformation of the final DFM due to the controlled reduction of perovskite-based formulation. With that aim, the temperature was progressively increased from room temperature to 650, 550 or 800 °C (2 h) for bulk and ceria- and alumina-supported samples, respectively. Note that the reduction temperature for each support was already optimized in a previous study [39].

Once the DFM was obtained, CO$_2$ adsorption and hydrogenation experiments were carried out, increasing the reaction temperature progressively from 280 to 520 °C, in steps of 40 °C. During the adsorption period (60 s), the feed composition was 10% CO$_2$/Ar. Then, this step was followed by a purge with Ar (120 s) to remove weakly adsorbed CO$_2$ and prevent mixing of streams. Finally, CO$_2$ was replaced by a 10% of H$_2$ during the hydrogenation (methanation) period (120 s). Before starting the following CO$_2$ adsorption period, the catalyst and the system were again purged with Ar for 60 s. The catalytic tests were carried out with a total flow rate of 1200 mL min^{-1}. This flow corresponds to space velocities of around 45,000 and 140,000 h^{-1} for ceria- and alumina-supported samples, respectively. CO$_2$, CH$_4$, CO and H$_2$O were continuously quantified by a *MKS MultiGas 2030 FT-IR* analyser.

The amount of CO$_2$ stored was calculated from Eq. (2). With that aim, the amount that leaves the reactor must be subtracted from the amount fed. To determine the amount of CO$_2$ fed, the stream from the feed system was led directly to the analyser. The obtained profile corresponds to the actual CO$_2$ input that was fed to the reactor.

$$STO_{CO_2} \; (\mu mol \; g^{-1}) = \frac{1}{W} \int_0^t \left[F_{CO_2}^{in}(t) - F_{CO_2}^{out}(t) \right] dt \qquad (2)$$

On the other hand, the CH$_4$, CO and H$_2$O productions were calculated from the following expressions:

$$Y_{CH_4} \; (\mu mol \; g^{-1}) = \frac{1}{W} \int_0^t F_{CH_4}^{out}(t) dt \qquad (3)$$

$$Y_{CO} \; (\mu mol \; g^{-1}) = \frac{1}{W} \int_0^t F_{CO}^{out}(t) dt \qquad (4)$$

$$Y_{H_2O} \; (\mu mol \; g^{-1}) = \frac{1}{W} \int_0^t F_{H_2O}^{out}(t) dt \qquad (5)$$

CH$_4$ selectivity is determined by relating the CH$_4$ and CO productions

since they were the only two products that were detected:

$$S_{CH_4}(\%) = \frac{Y_{CH_4}}{Y_{CH_4} + Y_{CO}} \times 100 \qquad (6)$$

Finally, the carbon balance check was carried out from the following expression:

$$CB(\%) = \left(\frac{Y_{CH_4} + Y_{CO}}{STO\_CO2}\right) \times 100 \qquad (7)$$

3. Results and discussion

3.1. Catalysts characterization

Fig. 1 includes XRD patterns of 30% LaNiO$_3$/CeO$_2$, 30% LaNiO$_3$/Al$_2$O$_3$ and 30% LaNiO$_3$/La-Al$_2$O$_3$ samples before (a) and after (b) CO$_2$ methanation reaction. The corresponding XRD diffractograms of ceria (CeO$_2$) and alumina (Al$_2$O$_3$) supports as well as of bulk perovskite (LNO) are also included as reference.

Regarding to fresh samples (Fig. 1a), intense diffraction peaks (○) at 28.6, 33.1, 47.5, 56.3 and 59.1 °2θ are observed for ceria support, whereas wide peaks (+) at 7.6, 45.9 and 67.0 °2θ are identified for alumina support. These reflections are characteristic of a cubic highly crystalline ceria and an amorphous cubic alumina phases, respectively. On the other hand, the bulk perovskite (LNO) shows three mains diffraction peaks (Δ) at 32.9, 47.4 and 58.7 °2θ, which are characteristic of a rhombohedral LaNiO$_3$ phase. Furthermore, this sample also shows additional peaks in form of impurities, characteristic of hexagonal La$_2$O$_2$CO$_3$ (●), cubic NiO (□) and tetragonal La$_2$NiO$_4$ (▲) phases, respectively. Their presence suggests that a fraction of Ni^{2+} and La^{3+} is not inserted inside the perovskite structure during perovskite structure conformation, due to a limited stability of LaNiO$_3$ oxide.

Supported samples (30% LaNiO$_3$/CeO$_2$, 30% LaNiO$_3$/Al$_2$O$_3$ and 30% LaNiO$_3$/La-Al$_2$O$_3$) show an intermediate diffractogram to that described for the bulk perovskite and the corresponding support. However, it is worth mentioning that the peaks of the ceria support overlap those of the perovskite in the case of the 30% LaNiO$_3$/CeO$_2$ sample. In any case, the

small displacement of the peak situated at 33.1 °2θ to lower 2θ positions with respect to bare ceria support suggests the coexistence of both phases in the supported samples (Figure S1). Finally, it can be noticed that the relative intensity of the characteristic diffraction peaks of La$_2$O$_2$CO$_3$ (●), NiO (□), and La$_2$NiO$_4$ (▲) impurities, increases for Al$_2$O$_3$- and La-Al$_2$O$_3$-supported samples with respect to bulk perovskite and CeO$_2$-supported samples. These results suggest that the LaNiO$_3$ conformation is partially limited over alumina-supported samples, especially for bare Al$_2$O$_3$ support.

Once LaNiO$_3$ perovskite is conformed, Ni should be ex-solved from the perovskite host with controlled size to conform the desired DFM. In order to confirm the Ni nanoparticles (NPs) ex-solution, XRD measurements were carried out for the samples used in cyclic CO$_2$ adsorption and in-situ hydrogenation (Fig. 1b). Note that these samples were in-situ reduced prior to the catalytic test at the temperatures specified in Section 2.3. As can be observed, all samples show intense diffraction peaks of corresponding supports (CeO$_2$ or Al$_2$O$_3$), which confirm their high stability. In contrast, no diffraction peaks are discernible for LaNiO$_3$, NiO and La$_2$NiO$_4$ phases. These results confirm the complete reduction of NiO, LaNiO$_3$ and La$_2$NiO$_4$ phases, leading to cubic Ni^0 (▣) and La$_2$O$_3$ formation. However, an increase in the intensity of La$_2$O$_2$CO$_3$ diffraction peaks is observed, instead of La$_2$O$_3$ phase identification. In agreement with that reported in previous works [40,41], this fact is due to CO$_2$ adsorption on La$_2$O$_3$ sites during CO$_2$ methanation. Hence, XRD results demonstrate the controlled ex-solution of Ni^0 nanoparticles from the LaNiO$_3$ during the controlled reduction process. Ultimately, DFMs are obtained with the following general formulation: Ni-La$_2$O$_3$/support (with support = Al$_2$O$_3$, La-Al$_2$O$_3$ or CeO$_2$).

The Ni^0 crystallite sizes are determined by applying the Scherrer equation to the peak located at 51.8 °2θ in the used samples (Table 1). As can be observed, the crystallite size of the 30% LNO/CeO$_2$ sample is 7.0 nm, whereas it increases to 12.4 and 11.5 nm for 30% LNO/Al$_2$O$_3$ and 30% LNO/La-Al$_2$O$_3$ samples, respectively. In agreement with XRD results (Fig. 1a), the ceria support favours the formation of a higher proportion of LaNiO$_3$ perovskite, instead of impurities; as a consequence, this fact increases the Ni^{3+} available to be ex-solved, in form of smaller
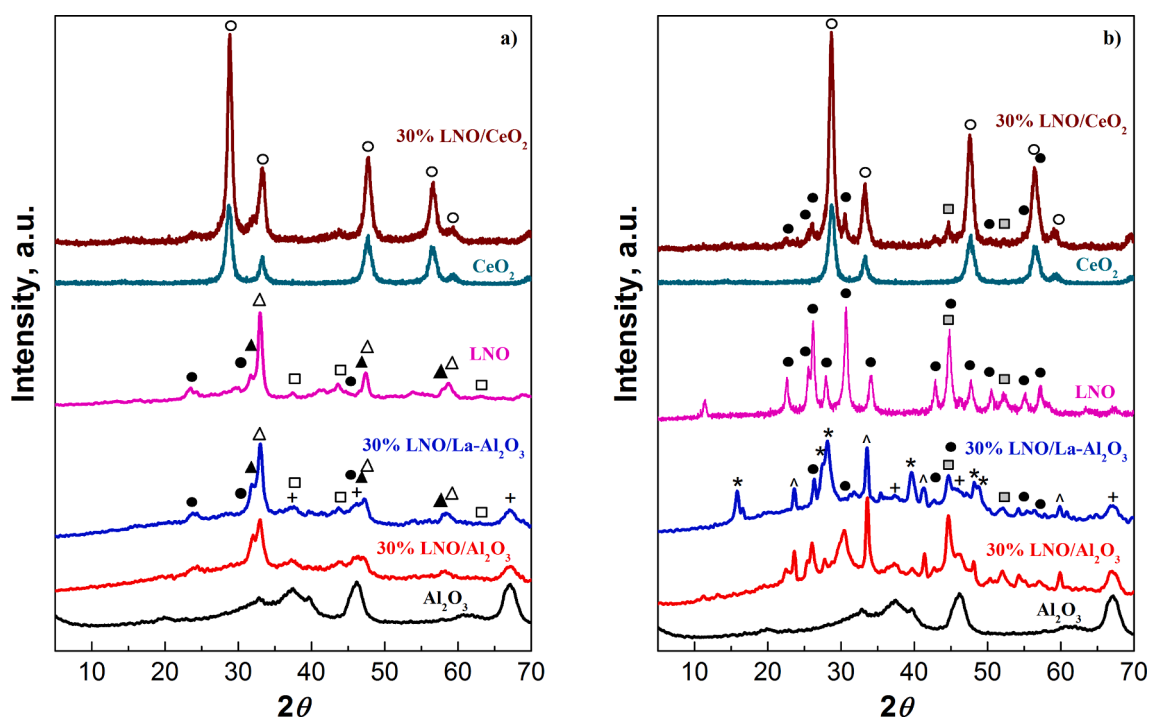

Fig. 1. XRD diffractograms of: a) fresh and b) reduced and used 30% LaNiO$_3$/CeO$_2$, 30% LaNiO$_3$/Al$_2$O$_3$ and 30% LaNiO$_3$/La-Al$_2$O$_3$ samples. LaNiO$_3$ perovskite, Al$_2$O$_3$ and CeO$_2$ supports are also included as reference. (●) La$_2$O$_2$CO$_3$, (○) ceria, (□) NiO, (▲) La$_2$NiO$_4$, (▣) Ni^0, (Δ) LaNiO$_3$, (+) Al$_2$O$_3$, (*) La(OH)$_3$ and (ˆ) LaAlO$_3$.

Table 1

Specific surface areas (S_{BET}), pore volumes (V_p), Ni content and Ni^0 crystallite sizes for the $LaNiO_3$, 30% $LaNiO_3/CeO_2$, 30% $LaNiO_3/Al_2O_3$ and 30% $LaNiO_3/La-Al_2O_3$ samples after reduction and CO_2 methanation reaction.

Sample	S_{BET}, m^2 g^{-1}	V_p, cm^3 g^{-1}	Ni, %	d_{Ni}, nm [a]
CeO_2	78	0.16	–	–
Al_2O_3	193	0.54	–	–
$La-Al_2O_3$	179	0.48	–	–
30% LNO/CeO_2	37 (47)	0.12 (0.17)	9.2	7.0
30% LNO/Al_2O_3	103 (118)	0.34 (0.36)	9.3	12.4
30% $LNO/La-Al_2O_3$	105 (116)	0.34 (0.36)	9.4	11.5
LNO	12 (21)	0.09 (0.12)	26.9	31.7

*In brackets are shown the corresponding values to fresh samples.

[a]Ni^0 crystal size estimated by Scherrer equation for reduced and used samples.

Ni^0 NPs, during the reducing step. In any case, these values are significantly lower than that observed for the bulk perovskite (31.7 nm). Thus, supporting the $LaNiO_3$ perovskite over different nature supports seems to be an efficient way to promote the ex-solution of Ni NPs with smaller crystallite size.

Different phase's distribution of 30% $LaNiO_3/CeO_2$, 30% $LaNiO_3/Al_2O_3$ and 30% $LaNiO_3/La-Al_2O_3$ used samples were analyzed by STEM-HAADF images and representative EDS elemental maps (Fig. 2). Furthermore, their Ni particle sizes distribution, estimated by measuring the size of at least 100 particles identified in these images, is also included in the form of a histogram. As a general trend, Ce (dark blue colour) or Al (light blue colour) and La (green colour) elements coexist with homogeneous distribution in all analyzed areas. Furthermore, small-sized Ni NPs (red colour) uniformly distributed on La and Ce or Al surface can be identified irrespective the analyzed support. Nevertheless, the Ni particle's agglomeration is higher for the alumina-supported samples (Fig. 2b and c), which leads to a more heterogeneous Ni particle

size distribution in the right side histogram. In agreement with the Ni size estimated by XRD experiment (Table 1), the lowest average size (5.0 nm) corresponds to 30% $LaNiO_3/CeO_2$ sample (Fig. 2a), whereas both alumina-supported samples show a Ni average size above 10 nm. These observations evidenced that the utilization of ceria as support favours the formation of a DFM with smaller Ni NPs. As previously suggested by XRD diffractograms (Fig. 1), the $LaNiO_3$ perovskite formation is favoured with respect to the formation of impurities (i.e. $La_2O_2CO_3$, NiO and La_2NiO_4), favouring the ex-solution of Ni^0 NPs with smaller size from the perovskite host. Furthermore, the ceria-supported sample requires lower reduction temperature (550 °C vs. 800 °C) to completely ex-solve the Ni^0 NPs from the different Ni-based phases, which limits their sintering during reduction step. Finally, these aspects seem to favour a more homogenous distribution of the La-based phases for ceria-supported samples.

The analysis of the main textural properties of the used samples was carried out by isothermal (–196 °C) N_2-adsorption–desorption. As expected, all perovskite-based formulations show type IV isotherms (Figure S2) according to the IUPAC classification, which are characteristic of mesoporous materials. Table 1 summarizes the corresponding specific surface areas (S_{BET}) and pore volumes (V_p) for the used and fresh samples (in brackets). 30% $LaNiO_3/CeO_2$, 30% $LaNiO_3/Al_2O_3$ and 30% $LaNiO_3/La-Al_2O_3$ samples present S_{BET} of 37, 103 and 105 m^2 g^{-1}, respectively. This trend is ascribed to the progressive overlap of the pores and the supports surface by the deposition of the $LaNiO_3$ perovskite, together with pores narrowing due to calcination as well as reduction at high temperatures, in line with the proportional decrease in pore volume observed. In any case, these values are much higher than that of the bulk perovskite (12 m^2 g^{-1}), which contributes to the ex-solution of smaller Ni NPs.

In order to investigate the redox properties of the samples, Fig. 3 shows the hydrogen consumption profiles, normalized per sample mass
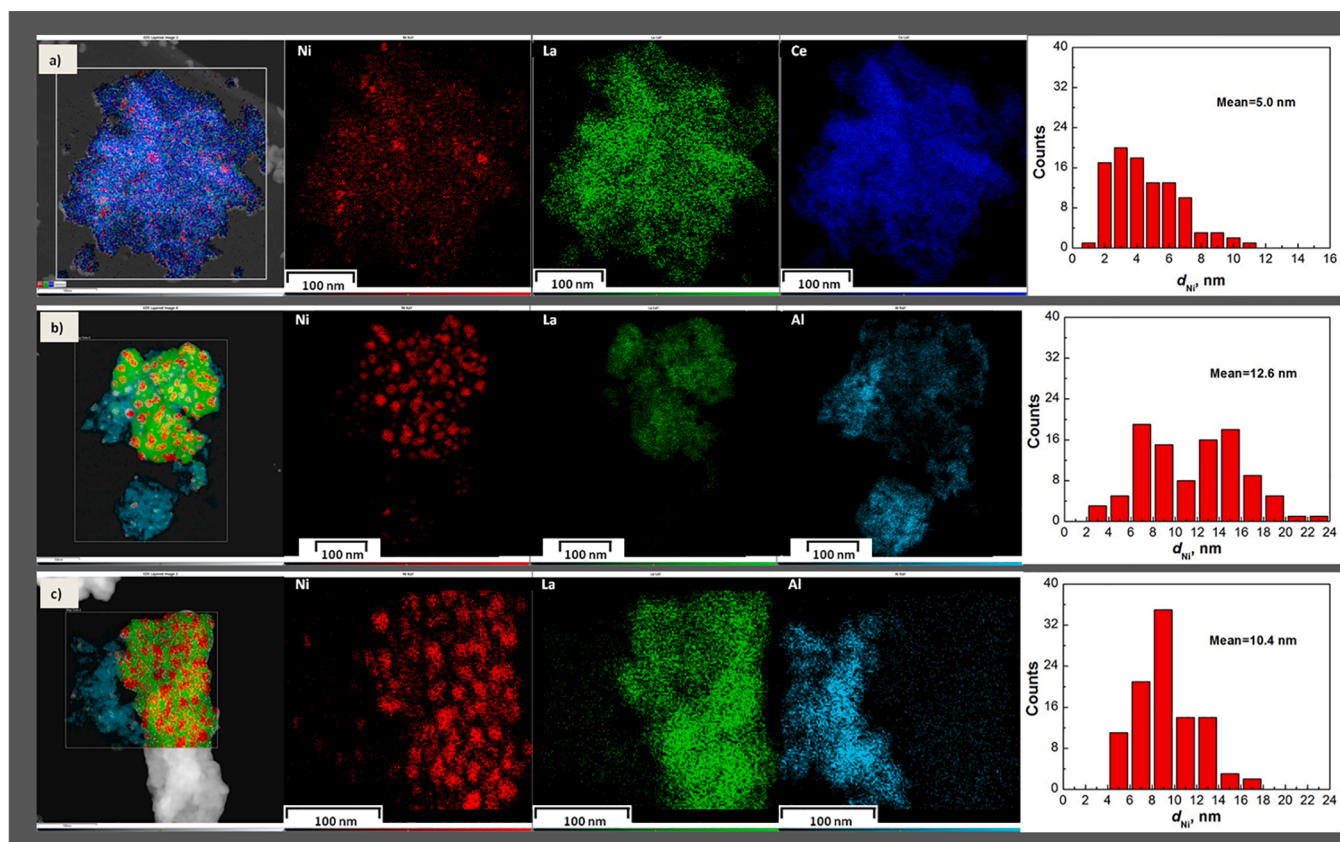

Fig. 2. STEM-HAADF images and the corresponding EDS maps obtained for: a) 30% $LaNiO_3/CeO_2$, b) 30% $LaNiO_3/Al_2O_3$ and c) 30% $LaNiO_3/La-Al_2O_3$ samples after controlled reduction and CO_2 methanation reaction. The Ni particle sizes distribution was also included for each sample in form histograms.
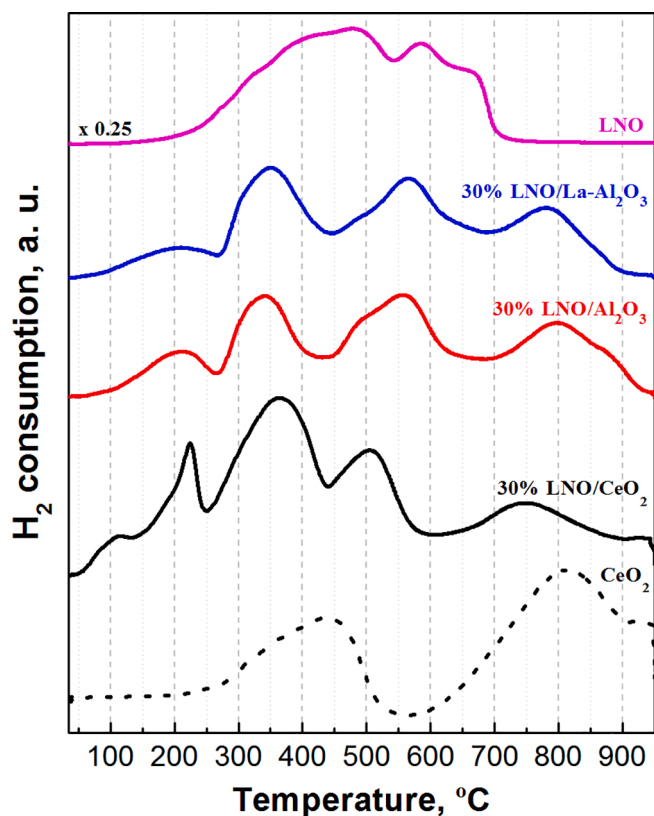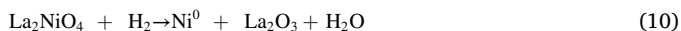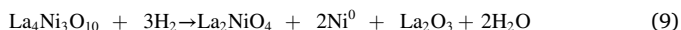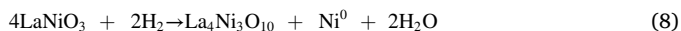
Fig. 3. H$_2$-TPR profiles normalized per sample mass of fresh: 30% LaNiO$_3$/ CeO$_2$, 30% LaNiO$_3$/Al$_2$O$_3$ and 30% LaNiO$_3$/La-Al$_2$O$_3$ samples. The reduction profiles of CeO$_2$ support and bulk LaNiO$_3$ perovskite (LNO) are included as reference.

unit, for fresh 30% LaNiO$_3$/CeO$_2$, 30% LaNiO$_3$/Al$_2$O$_3$ and 30% LaNiO$_3$/ La-Al$_2$O$_3$ samples. For comparative purposes, the H$_2$–TPR profiles of bulk LaNiO$_3$ perovskite (LNO) and CeO$_2$ support are also included.

In agreement with the results in our previous work [39], the ceria-supported perovskite shows an intermediate reduction profile between the CeO$_2$ support and bulk LaNiO$_3$ perovskite. Specifically, two main H$_2$ consumption regions can be identified, i.e. below and above 650 °C. As observed for the bulk LaNiO$_3$, the low temperature region presents three main peaks centred at 225, 375 and 475 °C, which are ascribed to the progressive reduction of NiO, LaNiO$_3$ and La$_2$NiO$_4$ phases following the stoichiometry of Eqs. (8–10). Note that the Ce^{4+} at the surface is also reduced in this temperature region. Meanwhile, the peak above 650 °C is ascribed to the final reduction of the bulk CeO$_2$ (Eq. (11)) [42].

$$4LaNiO_3 + 2H_2 \rightarrow La_4Ni_3O_{10} + Ni^0 + 2H_2O \qquad (8)$$

$$La_4Ni_3O_{10} + 3H_2 \rightarrow La_2NiO_4 + 2Ni^0 + La_2O_3 + 2H_2O \qquad (9)$$

$$La_2NiO_4 + H_2 \rightarrow Ni^0 + La_2O_3 + H_2O \qquad (10)$$

$$2CeO_2 + H_2 \rightarrow Ce_2O_3 + H_2O \qquad (11)$$

The reduction profiles of alumina-supported samples (30% LaNiO$_3$/ Al$_2$O$_3$ and 30% LaNiO$_3$/La-Al$_2$O$_3$) differ from that observed for ceria-supported sample. On the one hand, the reduction of NiO, LaNiO$_3$ and La$_2$NiO$_4$ phases (Eqs. 8–10) takes place more progressively. On the other hand, a new contribution, centred around 750–800 °C, is observed. Taking into account that Al$_2$O$_3$ and La-Al$_2$O$_3$ support are no reducible, this peak is associated with the reduction of highly stable NiAl$_2$O$_4$ phase formed during calcination step [43]. These results denote a high interaction between the Ni and alumina support, which limits the conformation of the perovskite oxide and favours the presence of impurities, as

previously suggested by XRD analysis (Fig. 1).

As can be observed, the reducibility is clearly enhanced for ceria-supported samples with respect to those observed for the bulk perovskite and the ceria support. In contrast, this shift is limited for the alumina-supported samples, especially for the perovskite deposited onto bare alumina. However, it is worth to mention that species below 250 °C are more easily reduced for alumina-supported samples than for ceria-supported and bulk perovskites. As previously suggested, the reduction of NiO, not inserted in the perovskite lattice, also occurs at this temperature region and is favoured by the higher specific surface area of alumina-supported samples with respect to the ceria-supported one. In any case, the concentration of the species reduced in the low temperature region (below 650 °C) is significantly higher for the ceria-supported samples. These results evidence that the redox properties of the samples are favoured with ceria as support, which leads to an easier reduction of Ni-based species as well as of ceria support [44]. Thus, synergetic effects between LaNiO$_3$ and ceria phases are evidenced, which promote the accessibility of the former and the reducibility of the latter due to spill-over effect of activated H$_2$ [32].

To gain insight on the hydrogen consumption occurred during H$_2$-TPR experiments, the effluent gas was analyzed by mass spectroscopy for ceria- and alumina-supported samples (Figure S3). As can be observed, a noticeable methane formation can be identified in both cases due to the hydrogenation (CO$_2$ + 4H$_2$ ⇌ CH$_4$ + H$_2$O) of the CO$_2$ released due to La$_2$O$_2$CO$_3$ decomposition on Ni^0 sites, specie formed during the perovskite reduction at lower temperatures. As a result, this process implies the consumption of additional H$_2$. Thus, the H$_2$ consumption observed between 250 and 600 °C is not only due to the reduction of reducible species but also due to the methane formation of the adsorbed CO$_2$ at the surface. Among different supports, the 30% LNO/CeO$_2$ sample shows the highest CH$_4$ production below 400 °C. This trend suggests that the activation of CO$_2$ methanation takes place at lower temperatures for the DFMs obtained from the ceria-supported sample, in line with the higher reducibility observed during H$_2$-TPR experiments (Fig. 3).

Table 2 shows the integrated area related to the reduction of the different species per gram of sample. Based on the reduction steps described in Eqs. (8–10), 1.5 mol of hydrogen are consumed per 1 mol of LaNiO$_3$ perovskite, whereas 0.5 mol of hydrogen are consumed in the reduction of CeO$_2$ support (Eq. (11)). In contrast, no hydrogen consumption is expected due to the La-Al$_2$O$_3$ or Al$_2$O$_3$ supports reduction.

Table 2

Deconvoluted H$_2$ consumption ascribed to the reduction of different species of the fresh CeO$_2$ support, bulk LaNiO$_3$ perovskite (LNO) and, 30% LaNiO$_3$/CeO$_2$, 30% LaNiO$_3$/Al$_2$O$_3$ and 30% LaNiO$_3$/La-Al$_2$O$_3$ samples.

Sample	NiO + LaNiO$_3$ [a], μmol H$_2$ g^{-1}	La$_4$Ni$_3$O$_{10}$ + CeO$_2$ (surf.) [b], μmol H$_2$ g^{-1}	La$_2$NiO$_4$ [c], μmol H$_2$ g^{-1}	CeO$_2$ (bulk)/ NiAl$_2$O$_4$ [d], μmol H$_2$ g^{-1}	Total [e], μmol H$_2$ g^{-1}
CeO$_2$	–	1626	–	3389	5015
30% LNO/ CeO$_2$	1087	2752	1310	2358	7507
30% LNO/ Al$_2$O$_3$	507	1122	1928	1187	4745
30% LNO/ La-Al$_2$O$_3$	376	1316	2022	871	4584
LNO	2722	8271	5225	–	16,218

[a] Sum of integrated peaks located below 250 °C.
[b] Sum of integrated peaks located between 250 and 450 °C.
[c] Sum of integrated peaks located between 450 and 650 °C.
[d] Sum of integrated peaks located above 650 °C.
[e] Sum of all integrated peaks.

Moreover, noticeable hydrogen consumption is related to carbonates reduction, in line with the high CH_4 production identified in Figure S3. In fact, this contribution should be more relevant for ceria-supported samples. As a result, the overall H_2 uptake decreases from 7507 µmol $H_2 g^{-1}$ for ceria-supported samples to values below 4745 µmol $H_2 g^{-1}$ for alumina-supported samples.

It is worth to mention that the increase in H_2 consumption for the 30% LNO/CeO_2 sample is especially remarkable below 400 °C (Table 2). In order to explore in more detail this aspect, Fig. 4 plots the evolution of the H_2 uptakes below 250 °C related to Ni content for different supported samples and bulk perovskite. Note that this hydrogen consumption was previously assigned to the partial reduction of Ni^{3+} in the perovskite lattice together with the reduction of highly dispersed NiO nanoparticles, since no CH_4 formation is observed in this temperature region (Figure S3). As can be observed, the H_2/Ni ratio progressively decreases from 0.82 for 30% LNO/CeO_2 sample to 0.23 for 30% $LNO/La-Al_2O_3$ sample. This result confirms that the H_2 activation during CO_2 methanation is promoted at lower temperatures by the use of ceria support due to the increase in the concentration of highly reducible Ni-based species in $LaNiO_3$ perovskite.

To investigate the interaction between the CO_2 molecule and the catalyst surface, the CO_2–TPD profiles of the $LaNiO_3$, 30% $LaNiO_3/CeO_2$ 30% $LaNiO_3/Al_2O_3$ and 30% $LaNiO_3/La-Al_2O_3$ samples, as well as those of the corresponding supports (CeO_2, Al_2O_3 and $La-Al_2O_3$) were compared (Fig. 5). Each sample was prereduced following a similar procedure to that achieved prior to catalyst test (Section 2.3). On the one hand, ceria support shows a single desorption peak centred at 100 °C, which is assigned to the CO_2 decomposition arising from bridged and bidentate carbonates adsorbed onto ceria surface. Meanwhile, the weak signal, observed above 400 °C, is assigned to the decomposition of carbonates not eliminated during calcination and reduction steps [45]. On the other hand, bare Al_2O_3 and $La-Al_2O_3$ supports present an asymmetric desorption peak at 100 °C, which is assigned to CO_2 desorption from weak Brönsted OH^- groups [43]. It is worth to note that the shoulder at higher temperatures is slightly higher for $La-Al_2O_3$ support, due to the CO_2 desorption from monodentate carbonates adsorbed on highly dispersed La_2O_3 formed on catalytic surface.

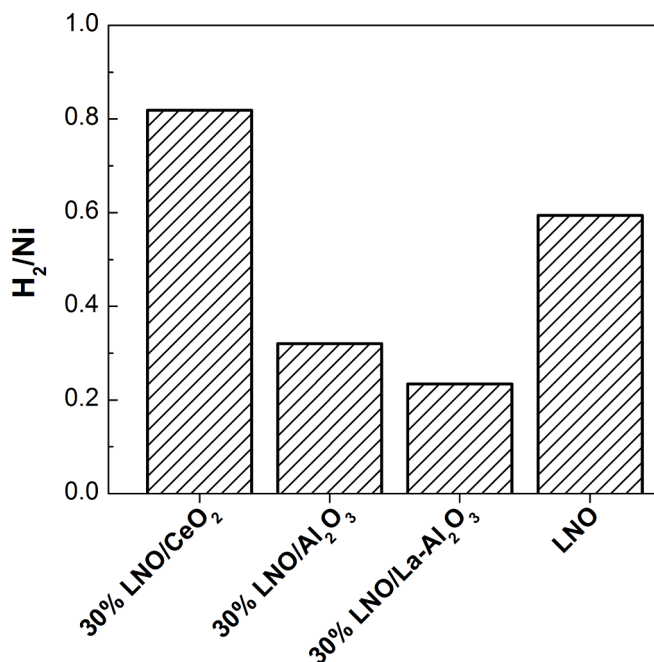Regarding bulk perovskite, three main desorption peaks can be
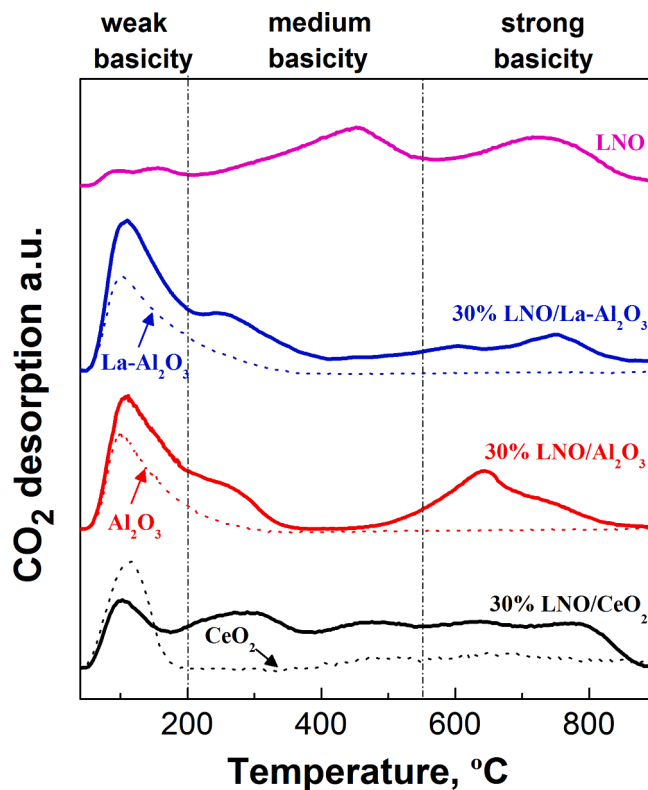
Fig. 5. CO_2-TPD profiles normalized per sample mass of reduced 30% $LaNiO_3/CeO_2$, 30% $LaNiO_3/Al_2O_3$, 30% $LaNiO_3/La-Al_2O_3$, $LaNiO_3$ samples, and CeO_2, Al_2O_3 and $La-Al_2O_3$ supports.

observed: below 200 °C, between 200 and 550 °C and above 550 °C. In increasing order of temperature, these peaks are assigned to the decomposition of weakly adsorbed CO_2 on Ni^0 sites [46], and decomposition of monodentate carbonates linked to highly dispersed and bulk-like La_2O_3 species in the form of $La_2O_2CO_3$ [27,44], respectively. As expected, supported perovskites show an intermediate CO_2 desorption profile to that observed for the bulk $LaNiO_3$ perovskite and the corresponding support. Nevertheless, two main differences can be identified. On the one hand, the desorption of the different adsorbed species takes place at lower temperatures with respect to bulk perovskite. On the other hand, a more progressive CO_2 decomposition during the whole temperature range is favoured for ceria-supported sample. As previously discussed, the impregnation of the $LaNiO_3$ perovskite on a high surface area supports limits its agglomeration during calcination. This fact promotes a more homogeneous distribution of the La_2O_3 phases at the surface, which favours the formation of monodentate carbonates of different stability on the La_2O_3 sites. However, this process is partially limited for alumina-supported samples due to the formation of $NiAl_2O_4$ in detriment of $LaNiO_3$ perovskite conformation, in line with XRD results (Fig. 1). This fact limits the ex-solution of La_2O_3 from the perovskite, favouring its sintering during the reduction at high temperatures, which ultimately leads to more heterogeneous distribution of the La_2O_3 phase than in ceria-supported samples (Fig. 2).

According to desorption temperature or chemical bond strength, basic sites can be classified into weak (T < 150 °C), medium (T = 200–550 °C) and strong (T > 550 °C). Based on this distribution, the concentration of the different species was determined after the deconvolution and integration of the different peaks identified in the desorption profile (Table 3). Comparing supported samples, the lower concentration of the weak basic sites corresponds to the reduced 30% $LaNiO_3/CeO_2$ sample. As observed in Table 1, this fact is ascribed to its lower specific surface area, which leads to almost total coverage of the ceria surface. In contrast, this sample shows significantly higher medium

Fig. 4. H_2 consumption (below 250 °C) related to Ni content for the fresh 30% $LaNiO_3/CeO_2$, 30% $LaNiO_3/Al_2O_3$ and 30% $LaNiO_3/La-Al_2O_3$ samples.

Table 3

Deconvoluted CO_2 desorption related to different basic sites, medium basic sites density and adsorbent utilization factor for bulk $LaNiO_3$ perovskite (LNO) and, 30% $LaNiO_3/CeO_2$, 30% $LaNiO_3/Al_2O_3$ and 30% $LaNiO_3/La-Al_2O_3$ samples after reduction in 5% H_2/Ar.

Sample	Weak basicity [a], µmol CO_2 g^{-1}	Medium basicity [b], µmol CO_2 g^{-1}	Strong basicity [c] µmol CO_2 g^{-1}	Total basicity [d], µmol CO_2 g^{-1}	Medium basic sites density[e], µmol CO_2 m^2	Ratio CO_2/ La_2O_3 [f]
30% LNO/ CeO$_2$	29.5 (49.6)	120.6 (8.0)	87.1 (26.2)	237.2 (84.4)	3.26 (0.10)	0.28
30% LNO/ Al$_2$O$_3$	74.2 (34.4)	29.0 (11.2)	58.5 (5.4)	161.7 (50.9)	0.28 (0.06)	0.20
30% LNO/La-Al$_2$O$_3$	93.8 (52.7)	41.1 (21.0)	46.9 (3.6)	182.3 (77.3)	0.39 (0.12)	0.20
LNO	11.6	75.0	73.3	159.5	6.25	0.08

*In brackets are shown the corresponding values to each support (CeO_2, Al_2O_3 and $La-Al_2O_3$).

[a] Sum of integrated peaks located below 200 °C.
[b] Sum of integrated peaks located between 200 and 550 °C.
[c] Sum of integrated peaks located above 550 °C.
[d] Sum of all integrated peaks.
[e] Determined as the µmoles of CO_2 desorbed between 200 and 550 °C per specific surface area.
[f] Moles of CO_2 desorbed, once the amount desorbed from the corresponding support was subtracted, per mol of La_2O_3.

and strong basic sites concentration than alumina-supported samples (30% $LaNiO_3/Al_2O_3$ and 30% $LaNiO_3/La-Al_2O_3$). Specifically, the concentration of medium and strong basic sites ranges from 120.6 and 87.1 µmol CO_2 g^{-1} for the 30% LNO/CeO_2 sample to 29.0 and 58.5 µmol CO_2 g^{-1} for the 30% LNO/Al_2O_3 sample, respectively. As suggested in our previous work [39], the controlled reduction of 30% $LaNiO_3/CeO_2$ sample leads to the formation of additional medium strength basic sites (NiO-CeO_2 interface) for CO_2 adsorption with respect to alumina-supported samples and bulk perovskite. Furthermore, the high interaction of Ni with the support leads to the presence of $NiAl_2O_4$ phase (Fig. 3), which limits the $LaNiO_3$ perovskite conformation, increases the proportion of impurities (La_2O_3 and NiO) for fresh samples (Fig. 1a), and needs a higher reduction temperature (800 °C vs. 550 °C). Ultimately, these aspects limit the ex-solution of highly dispersed La_2O_3 basic sites from $LaNiO_3$ host, leading to a significant decrease of the concentration of medium strength basic sites.

In order to gain insight on this issue, Table 3 shows the ratio of desorbed moles of CO_2 per mol of La_2O_3. Note that for the accurate determination of the amount desorbed from the La_2O_3 adsorbent, the moles of CO_2 desorbed from the corresponding support were subtracted. According to decomposition reaction of lanthanum carbonate ($La_2O_2CO_3 \rightleftharpoons La_2O_3 + CO_2$) 1 mol of CO_2 should be desorbed per mol of La_2O_3, if this compound was completely carbonated during saturation step. However, this ratio is below 1 for all samples. Among them, the lowest value (0.08) corresponds to $LaNiO_3$ perovskite, whereas supported perovskites show values more than twice of that of bulk counterpart. Although ceria supported sample show significantly lower specific surface area (Table 1), it presents the highest value (0.28). This trend confirms the higher accessibility of La_2O_3 sites and the presence of additional CO_2 adsorption sites in the NiO-CeO_2 interface (180–360 °C). Finally, this fact leads to a significant increase of the surface density of medium basicity species, from 0.39 µmol CO_2 m^{-2} for alumina-supported samples to 3.26 µmol CO_2 m^{-2} for ceria-supported one. Thus, these results confirm that supporting $LaNiO_3$ perovskite over ceria support increases the accessibility and the concentration of CO_2 adsorption sites with respect to alumina-supported samples.

3.2. Catalytic activity in CO_2 adsorption and hydrogenation to CH_4

3.2.1. CO_2 adsorption and hydrogenation mechanism

Aiming to introduce the basic principles of the operation, Fig. 6 displays the evolution with time of the outlet concentration of CO_2, CH_4, CO and H_2O during an entire CO_2 adsorption and hydrogenation cycle at 400 °C. Although these results correspond to the DFM derived from 30% $LaNiO_3/CeO_2$ formulation, the global reaction evolution is similar for alumina-supported samples and bulk perovskite.
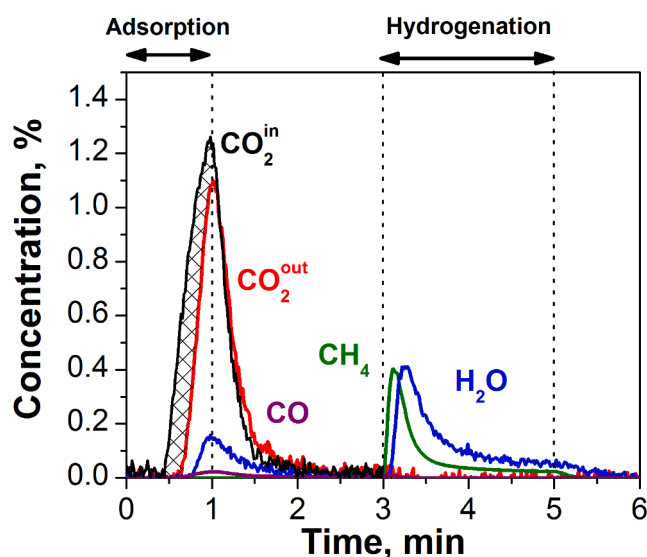

Fig. 6. CO_2, CH_4, H_2O and CO concentration profiles during a complete CO_2 adsorption and hydrogenation to CH_4 cycle at 400 °C for the DFM obtained after the controlled reduction of the 30% $LaNiO_3/CeO_2$ precursor.

During the adsorption cycle (1 min) a gas stream composed of 1.4% CO_2/Ar is fed. To estimate the amount of CO_2 adsorbed on the catalyst, the CO_2 concentration profile when the reactor is bypassed is also included. As can be observed, CO_2 concentration is almost negligible at the beginning of the adsorption period; in fact, no CO_2 signal at the reactor outlet is detected during the first 35 s. Following, it increases rapidly achieving almost the inlet concentration at the end of the storage period. This trend reveals the progressive CO_2 adsorption on storage sites, mainly La_2O_3 phase [47] and, in minor extent, on NiO–CeO_2 interface, up to their total saturation through the following reaction:

$$La_2O_3 \ + \ CO_2 \rightleftharpoons La_2O_2CO_3 \tag{12}$$

Few seconds delayed, an increasing H_2O signal is detected at the reactor outlet. The identification of this compound during the adsorption period reveals that CO_2 is progressively displacing pre-adsorbed H_2O due to its competitive adsorption on La_2O_3 storage sites through Eq. (13). However, it can be concluded that the CO_2 adsorption preferentially occurs onto free La_2O_3 sites, since H_2O is detected quite delayed with respect to CO_2 identification. Once La_2O_3 adsorption sites are completely carbonated (Eq. (12)), the storage of CO_2 is transferred to $La(OH)_3$ sites (Eq. (13)).

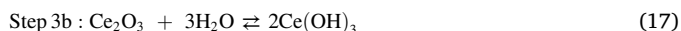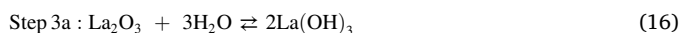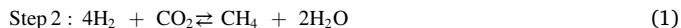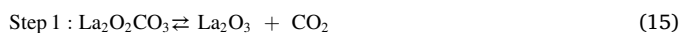$$2La(OH)_3 + CO_2 \rightleftarrows La_2O_2CO_3 + 3H_2O \qquad (13)$$
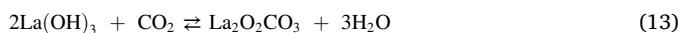
Note that the desorption of a small fraction of H_2O stored on ceria or alumina supports in form of hydroxyls cannot be ruled out, which can conform bicarbonates during CO_2 adsorption period. However, it is well-known that their stability is limited at working temperatures, which makes this adsorption route minority with respect to that expressed by Eqs. (12–13), especially for the ceria-supported sample [38].

From these data, the amount of CO_2 adsorbed onto the catalyst is calculated by Eq. (2) (Table 4). In order to assess the stable behavior of the DFM, the corresponding values to 3 consecutive cycles is included, which results in values between 86.4 and 90.7 μmol CO_2 g^{-1}. Furthermore, an almost negligible CO peak is observed during the adsorption period, which value is determined by Eq. (4) and summarized in Table 4 (around 9 μmol g^{-1}), which is related to the incomplete hydrogenation of adsorbed CO_2 with H_2 chemisorbed on the Ni^0 sites during the previous hydrogenation period following the reverse water gas shift reaction (RWGS, Eq. (14)). Alternatively, other authors related CO formation to the progressive decomposition of adsorbed formate species [48].

$$H_2 + CO_2 \rightleftarrows CO + H_2O \qquad (14)$$

Once the adsorption period is completed, the CO_2 is removed from the feed stream and a constant Ar flow rate is fed during 2 min, in order to purge the catalyst as well as the reaction system. As a result, CO_2 and H_2O signals progressively decrease practically to zero during this period.

Then, the hydrogenation period (2 min) begins with the admission of a gas stream composed of 10% H_2/Ar. Immediately after the injection of 10% H_2/Ar mixture, a sudden CH_4 production is observed with a long tail extended during the rest of the period. Besides, H_2O formation is detected around 10 s delayed from CH_4 detection. This process can be described by the following reaction scheme:

$$\text{Step 1}: La_2O_2CO_3 \rightleftarrows La_2O_3 + CO_2 \qquad (15)$$

$$\text{Step 2}: 4H_2 + CO_2 \rightleftarrows CH_4 + 2H_2O \qquad (1)$$

$$\text{Step 3a}: La_2O_3 + 3H_2O \rightleftarrows 2La(OH)_3 \qquad (16)$$

$$\text{Step 3b}: Ce_2O_3 + 3H_2O \rightleftarrows 2Ce(OH)_3 \qquad (17)$$

Firstly, lanthanum oxide carbonate is decomposed to form gaseous CO_2 (Eq. (15)). Then, the CO_2 released reacts with hydrogen to form methane and water following Sabatier reaction (Eq. (1)). Taking into account the stoichiometry of Eq. (1), 2 mol of H_2O should be detected per mol of CH_4; nevertheless, the experimental ratio during

hydrogenation period ranges between 1.38 and 1.40, which reveals that part of H_2O is stored on the surface La_2O_3 sites (Eq. (16)) or ceria support (Eq. (17)). As we already reported in previous work for conventional Ni/CeO_2 catalysts [49], the water adsorption on ceria sites is limited due to its high oxygen mobility, which favours water desorption during the hydrogenation period. Indeed, the H_2O/CH_4 ratio is significantly higher than that observed for conventional Ru-CaO/Al_2O_3 and Ru-Na_2CO_3/Al_2O_3 DFMs ($H_2O/CH_4 < 1.14$) [13]. Finally, a small fraction of CO (around 1 μmol g^{-1}) is also detected during the hydrogenation period due to RWGS reaction (Eq. (14)).

If the entire CO_2 adsorption and hydrogenation cycle is considered, a H_2O/CH_4 ratio ranging between 2.00 and 2.03 is obtained, that is close to the stoichiometry value ($H_2O/CH_4 = 2$) defined by Sabatier reaction (Eq. (1)). With the aim of giving more reliability to the results obtained, the carbon balance was also determined (Eq. (7)). As can be observed in Table 1, the amount of CO_2 stored during the adsorption period is around 88 μmol g^{-1}, whereas around 80 μmol g^{-1} of CH_4 and 8 μmol g^{-1} of CO are produced during CO_2 hydrogenation period. Thus, carbon balance closed within ± 5% since CH_4 and CO are the only products detected by FTIR during the reaction.

3.2.2. Support effect on CO_2 adsorption and hydrogenation cycles of $LaNiO_3$-derived DFMs

Catalytic activities of $LaNiO_3$-derived DFMs are evaluated by analyzing the evolution of CH_4 and CO production per cycle with reaction temperature (Fig. 7). These parameters were estimated applying Eqs. (2–3) for the data obtained from similar CO_2 adsorption and hydrogenation experiments to that reported in Fig. 6. Aiming to mimic an effluent gas from a combustion process, the CO_2 concentration during storage period was increased from 1.4 to 10% in these experiments, in which the carbon balance closed with an error below 5%.

As can be observed in Fig. 7a, the evolution of CH_4 production with reaction temperature is influenced by the type of perovskite-based formulation used as precursor of the corresponding DFM in each experiment. As expected, methane production increases up to 440 °C for DMFs obtained after the reduction of bulk $LaNiO_3$ and 30% $LaNiO_3$/CeO_2 formulations. Above this temperature, CO_2 conversion slightly decreases due to a destabilization of adsorbed carbonates. In contrast, DFMs obtained from alumina-supported perovskites (30% $LaNiO_3$/Al_2O_3 and 30% $LaNiO_3$/La-Al_2O_3) achieve their maximum CH_4 production at 280 °C. Then, a progressive decrease in the amount of CH_4 produced is observed at increasing temperatures. As previously observed, weak strength basic sites are predominant for alumina-supported DFMs (Table 3). Thus, the maximum CH_4 production observed at 280 °C is related to a more efficient CO_2 adsorption on weak strength basic sites, main adsorption sites at this temperature range. On the contrary, as the reaction temperature increases, the adsorbed CO_2 on weak basic sites become less stable, limiting their hydrogenation for alumina-supported samples. Meanwhile, the presence of higher strength basic sites for non– and ceria-supported samples favours decomposition of a major quantity of the adsorbed CO_2 species to be hydrogenated to CH_4 at higher temperatures. Thus, Ni-La_2O_3 interface higher accessibility can be considered as a key parameter to maximize CO_2 adsorption and in-situ hydrogenation at this temperature range.

Regarding to CO formation (Fig. 7b), all samples show an increasing CO production with reaction temperature. This trend is ascribed to the promotion of the RWGS reaction (Eq. (17)) during the CO_2 hydrogenation step. In any case, the CO production is below 31 μmol g^{-1} for all samples, which remarks the high selectivity towards methane of here developed materials.

Among different samples, the DFM obtained after the reduction of the $LaNiO_3$ formulation exhibits the highest CH_4 production (117 μmol g^{-1}), in line with the higher density of medium basic sites identified in Table 3. However, the DFM derived from 30% $LaNiO_3$/CeO_2 precursor maintains the highest CH_4 production, if the whole temperature range is considered. Furthermore, this sample shows a CO production 3 times

Table 4
Catalytic parameters estimated during 3 consecutive CO_2 adsorption and hydrogenation cycles at 400 °C with 30% $LaNiO_3$/CeO_2 catalyst.

	period	STO_{CO2}[a], μmol g^{-1}	CH_4[b], μmol g^{-1}	CO[c], μmol g^{-1}	H_2O[d], μmol g^{-1}	CB[e], %	H_2O/CH_4 ratio[f]
cycle 1	ads.	88.9	0.0	9.0	63.7	102.0	2.03
	hyd.	–	80.8	1.0	115.3		
cycle 2	ads.	86.4	0.0	9.0	62.8	104.6	2.00
	hyd.	–	80.4	1.0	113.0		
cycle 3	ads.	90.7	0.0	8.9	64.3	99.0	2.02
	hyd.	–	80.0	0.9	111.8		

[a] Stored CO_2 during the adsorption and hydrogenation steps together with the following purging period.
[b] Produced CH_4 during adsorption and hydrogenation steps.
[c] Produced CO during adsorption and hydrogenation steps.
[d] Released H_2O during the adsorption and hydrogenation steps together with the following purging period.
[e] Carbon balance during the entire CO_2 adsorption and hydrogenation process.
[f] H_2O to CH_4 ratio during the entire CO_2 adsorption and hydrogenation process.
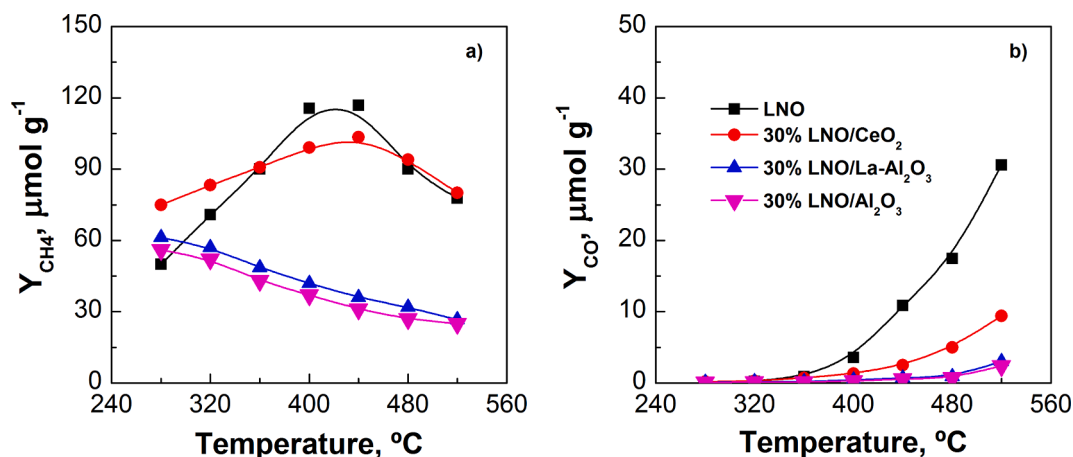
Fig. 7. Evolution of: a) CH_4 and b) CO productions with temperature for DFMs obtained after the controlled reduction 30% $LaNiO_3/CeO_2$, 30% $LaNiO_3/La-Al_2O_3$, 30% $LaNiO_3/Al_2O_3$ and $LaNiO_3$ precursors.

lower (8 vs. 31 µmol g^{-1}) than the DFM obtained from bulk perovskite, which is ascribed to the higher strength of CO_2 adsorbed species [50,51].

To better understand the differences in the catalytic behaviour, Fig. 8 plots CH_4 concentration profiles during complete CO_2 adsorption and hydrogenation cycles at 280, 400 and 520 °C for DFMs obtained from 30% $LaNiO_3/CeO_2$, 30% $LaNiO_3/La-Al_2O_3$ and $LaNiO_3$ precursors. Profiles corresponding to the 30% $LaNiO_3/Al_2O_3$ precursor have not been included since they are similar to those of La-Al$_2$O$_3$-supported sample. In general, the evolution of CH_4 is significantly affected by DFM composition, especially at intermediates-high temperatures. The maximum CH_4 production is observed at initial times for the alumina-supported sample, whereas this process is delayed and takes place more progressively for the DFM obtained from bulk perovskite. On the other hand, the ceria-supported sample shows an intermediate CH_4 production profile. As previously observed in Table 1, the specific surface area was significantly higher for supported samples with respect to that observed for the DFM derived from bulk perovskite, which leads to the exsolution of Ni NPs with significantly lower average particle size than bulk counterpart (31.7 nm), especially for ceria-supported sample. Furthermore, this sample shows the higher proportion of medium basic sites with respect to strong basic sites. Taking into account that the close contact between storage component and the Ni^0 NPs is regarded as the key factor to efficiently transfer of dissociated H to desorb, and subsequently to hydrogenate, adsorbed CO_2, these facts explain the wider temperature window of the DFM derived from the 30% $LaNiO_3/CeO_2$ formulation. In contrast, the stability of adsorbed species is limited for alumina-supported sample, favouring only the CH_4 production at the beginning of the hydrogenation period and low temperatures.

To sum up, the 30% $LaNiO_3/CeO_2$ emerges as the optimal catalytic precursor, resulting in a dual function material with high efficiency to adsorb CO_2 and in-situ hydrogenate it to methane. This fact is ascribed to an proper balance of different basic sites concentration, where CO_2 adsorption takes places (Ni-CeO$_2$ interface as well as highly dispersed and bulk-like La$_2$O$_3$), and higher accessibility of active sites for H$_2$ activation and CO_2 methanation (Ni^0 NPs). Ultimately, this fact also favours a higher selectivity towards methane. Furthermore, this sample is able to produce a high fraction of methane at initial period of the hydrogenation cycle. As suggested in our previous works [52,53], the duration of the hydrogenation period should be enough to ensure high CH_4 production but not too long to limit hydrogen conversion. Hence, optimal hydrogenation time will provide a best balance between more efficient use of reductant agent and CH_4 production. As a result, the faster kinetics discovered with the DFM derived from 30% $LaNiO_3/CeO_2$ catalytic precursor, makes it a first-class alternative as promotes the joint optimization of H$_2$ conversion and CH_4 production. The last aspect to consider is that the Ni content is around 70% lower with respect to

bulk $LaNiO_3$, which reveals a superior intrinsic activity of this sample.

In order to have a more realistic view of the relevance of the reported results, the CH_4 and CO productions obtained with this DFM where compared to those obtained with 15% Ni-15% CaO/Al$_2$O$_3$ model DFM (Figure S4) [13], showing comparable CO_2 adsorption and in-situ hydrogenation to CH_4. These results remark that here developed DFMs can be considered as promising novel materials for CO_2 methanation technology. The still limitation of higher CH_4 production at higher temperatures is actually under study in our labs with the use of other alkaline or earth-alkaline adsorbents, such as Ca, Ba, Na and K.

3.2.3. Evaluation of the real-world applicability of LaNiO$_3$-derived DFMs

The real-world applicability of the DFM obtained after the controlled reduction of 30% $LaNiO_3/CeO_2$ precursor was more deeply analyzed by subjecting this DFM to long-term CO_2 adsorption/hydrogenation experiments under hard operational conditions. This study was completed by evaluating the influence of the presence of O$_2$ during adsorption period on its CO_2 adsorption and hydrogenation efficiency.

Fig. 9 shows the evolution of CH_4 and CO productions with the number of CO_2 adsorption/hydrogenation cycles for 30% $LaNiO_3/CeO_2$-derived sample at 520 °C. As can be observed, CH_4 and CO productions as well as selectivity towards methane remain almost stable irrespective of time elapsed. Specifically, the CH_4 production slightly decreases from 80 µmol g^{-1} to 78.4 µmol g^{-1}, whereas CO production keeps at 9.3–9.4 µmol g^{-1}. This catalytic behaviour reveals the high stability of the developed DFM towards CO_2 adsorption and hydrogenation in consecutive cycles. The close contact between Ni^0 NPs, La$_2$O$_3$ and CeO$_2$ phases (Fig. 2), formed after the controlled reduction of 30% $LaNiO_3/CeO_2$, prevents the thermal agglomeration of Ni NPs during calcination and CO_2 methanation reaction processes, in line with the observed by Wang et al. [35] for Ni-La$_2$O$_3$/SBA-15 catalyst.

The developed DFM should also selectively capture CO_2 from O$_2$-containing flue gas at relatively high temperatures and then, hydrogenate the adsorbed species to methane with H$_2$. With the aim of evaluating the influence of the presence of O$_2$ during storage period a 10% of O$_2$ is jointly fed with a 10% of CO_2 during adsorption cycles. Fig. 10 plots the evolution of CH_4 and CO productions with the number of CO_2 adsorption/hydrogenation cycle at 400 °C for 30% $LaNiO_3/CeO_2$-derived sample. Note that the cycles 1–2 and 8–9 were carried out in the absence of O$_2$ in the feed stream, whereas this compound was fed in cycles 3–7.

Comparing cycles 1–2 with cycles 3–7, a negative effect on CH_4 production can be detected for the experiments in the presence of O$_2$ during the adsorption period. Indeed, the CH_4 yield immediately decreases from 99 to 47 µmol g^{-1} from the 2nd to 3rd cycle, whereas no significant changes are observed for cycles 4–7. Zheng et al. [54]
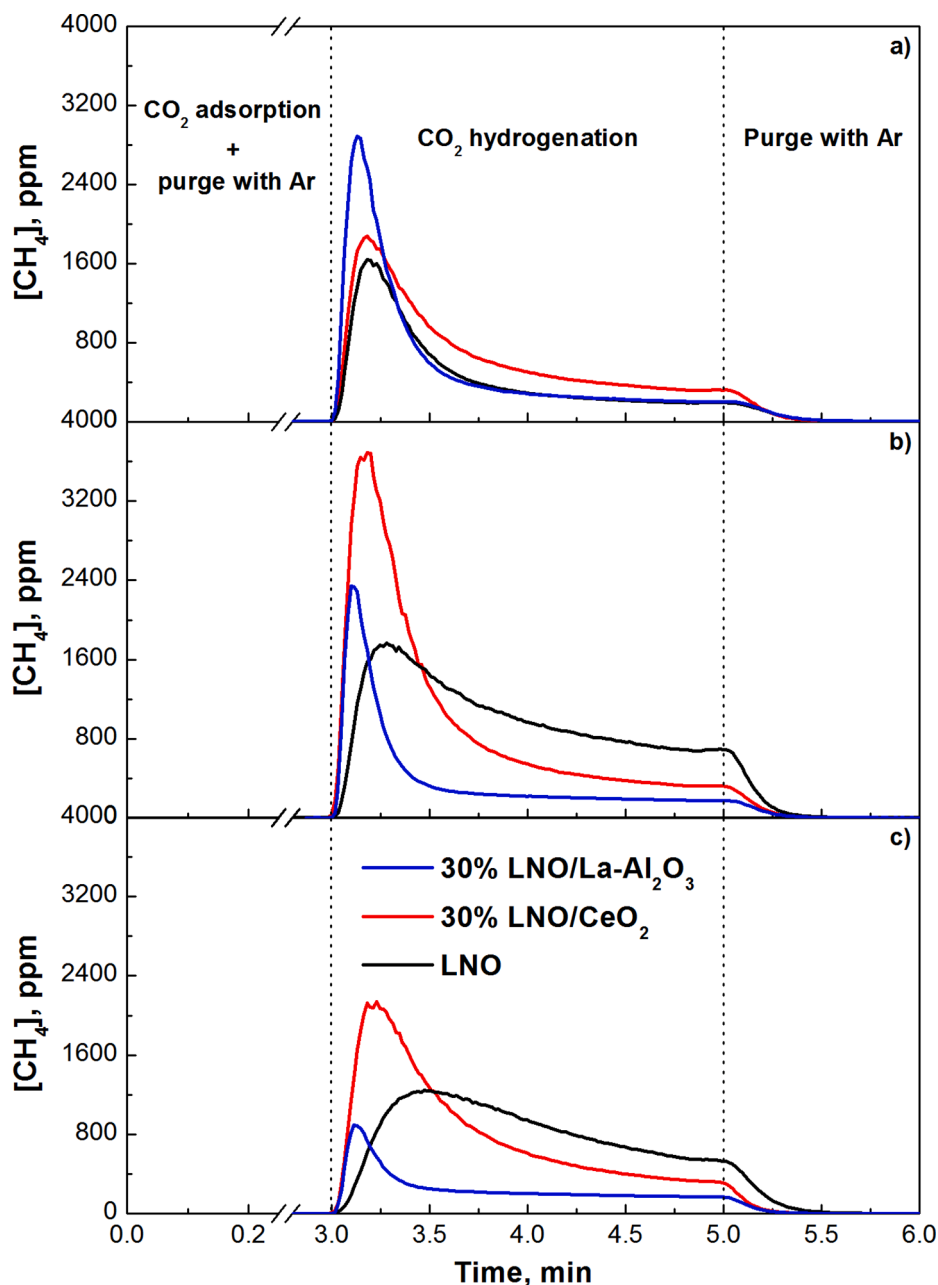
Fig. 8. CH₄ concentration profiles during a complete CO₂ adsorption and hydrogenation to CH₄ cycle at: a) 280, b) 400 and c) 520 °C for the DFMs obtained after the controlled reduction of 30% LaNiO₃/CeO₂, 30% LaNiO₃/La-Al₂O₃ and LaNiO₃ precursors.

justified the loss of activity for O_2-containing experiments by the oxidation of the active metallic phase during the adsorption step. In agreement with their results, a small CO_2 signal and a significant decrease in methane production is observed at the beginning of the hydrogenation period for the oxygen-containing experiment with respect to oxygen-free experiment (Figure S5). This fact reveals that some carbonates, adsorbed during the storage period, are released without being hydrogenated due to the absence of enough Ni^0 active sites to reduce them towards CH₄. In any case, the decrease in methane production for O_2-containing experiments is significantly lower to that observed for 10% Ni-6.1% NaO/Al₂O₃, where no methane formation was observed when the sample was exposed to O_2 and H_2O during the CO_2 capture step [19]. On the other hand, it is worth to mention that, in contrast to that observed in our previous work for conventional 10% Ni–10% Na₂CO₃/Al₂O₃ [11], CO production remains invariable after inclusion of O_2 in the feed stream. This trend discards the promotion of

RWGS reaction (Eq. (14)) due to a partial oxidation of Ni^0 to NiO.

During the next cycles (i.e. from the 8th to the 9th), CO_2 adsorption/hydrogenation cycles were again carried in an oxygen-free environment. Remarkably, the CH₄ production is recovered immediately after the oxygen is removed from the feed stream. Note that the 8th and 9th cycles show similar CH₄ and CO productions than 1st and 2nd cycles. Thus, these results reveal that the here discovered DFM has a high ability to restore activity once O_2 is not fed during CO_2 adsorption, which it is one of the main limitations of the conventional Ni-based formulations [19,55,56]. In agreement with the H₂-TPR results, the high reducibility of different Ni species implies that Ni can be easily reduced back during the hydrogenation step at low temperature. Therefore, 30% LaNiO₃/CeO₂-derived DFM can be considered a superior candidate for real conditions process at intermediate-high temperatures.

In summary, the confinement of Ni NPs on La₂O₃ or La-Ce-O interfaces prevents them from thermal agglomeration and favours their
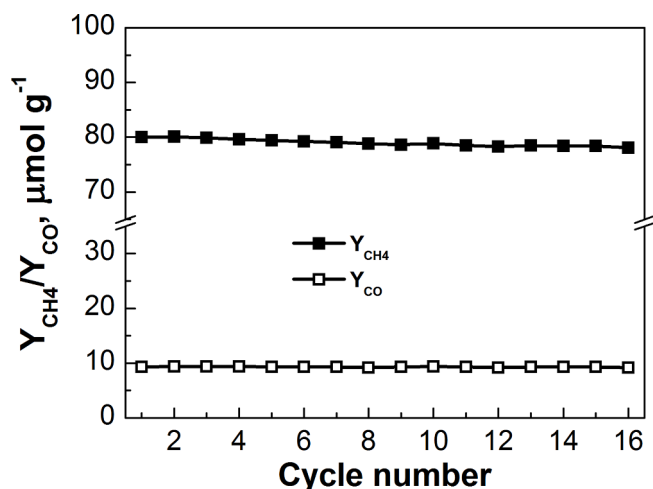
Fig. 9. Evolution of CH$_4$ and CO productions during the stability test (16 cycles at 520 °C) for the DFM obtained after the controlled reduction of the 30% LaNiO$_3$/CeO$_2$ precursor.
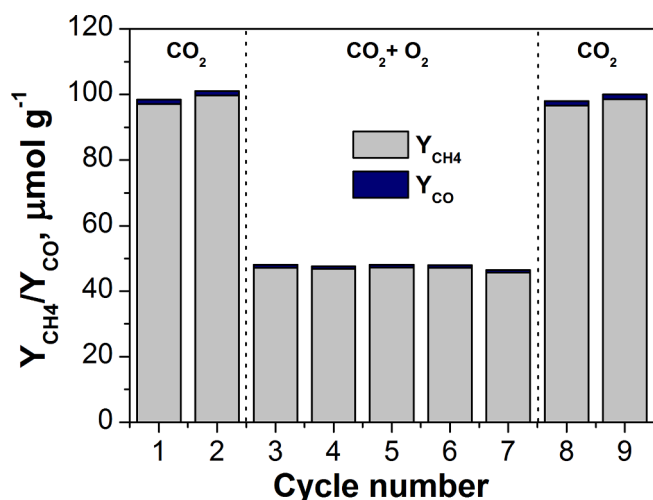

Fig. 10. CH$_4$ and CO productions during CO$_2$ adsorption and hydrogenation to CH$_4$ at 400 °C without (cycles 1–2 and 8–9) and with (cycles 3–7) O$_2$ during the adsorption step for the 30% LaNiO$_3$/CeO$_2$ DFM. The feed was 10% CO$_2$/Ar or (10% CO$_2$ + 10% O$_2$)/Ar (1 min) in the adsorption step and 10% H$_2$/Ar (2 min) in the hydrogenation step.

redox properties. Hence, ceria-supported LaNiO$_3$ perovskites can be considered as an efficient precursor of highly stable and versatile dual function materials for the cyclic CO$_2$ adsorption and hydrogenation to methane technology.

4. Conclusions

This work is focused on the analysis of the viability of LaNiO$_3$-based formulations as precursor of active, stable and versatile dual function materials for CO$_2$ adsorption and hydrogenation into CH$_4$. In particular, the following perovskite-based formulations are prepared by combining citric acid and wetness impregnation: LaNiO$_3$, 30% LaNiO$_3$/CeO$_2$, 30% LaNiO$_3$/Al$_2$O$_3$ and 30% LaNiO$_3$/La-Al$_2$O$_3$. The prepared formulations are widely characterized before and after controlled reduction process. XRD experiments reveal the presence of LaNiO$_3$ as well as of impurities in form of La$_2$O$_2$CO$_3$, NiO and La$_2$NiO$_4$ for all calcined samples. The concentration of these impurities increases for 30% LaNiO$_3$/Al$_2$O$_3$ and

30% LaNiO$_3$/La-Al$_2$O$_3$ samples with respect to LaNiO$_3$, 30% LaNiO$_3$/CeO$_2$ ones, whereas the specific surface area follows the opposite trend. Among different samples that supported on ceria oxide (30% LaNiO$_3$/CeO$_2$) shows the higher reducibility in H$_2$-TPR experiments, whereas the redox properties are limited for 30% LaNiO$_3$/Al$_2$O$_3$ and 30% LaNiO$_3$/La-Al$_2$O$_3$ due to the higher perovskite-support interaction, which favours the NiAl$_2$O$_4$ formation instead of LaNiO$_3$ conformation.

After the controlled reducing process, Ni is exsolved from perovskite host in developed formulations, leading to the formation of a mix between Ni^0 nanoparticles and La$_2$O$_3$ phase. However, the interaction of Ni nanoparticles with the La$_2$O$_3$ phase and support is controlled by the characteristic of the precursor used. The best compromise between specific surface area and LaNiO$_3$ stability observed for ceria-supported sample (30% LaNiO$_3$/CeO$_2$) promotes the formation of smaller Ni^0 nanoparticles and a more homogeneous La$_2$O$_3$ distribution. As a result, the obtained DFM presents a stronger interaction between Ni^0 NPs and the La$_2$O$_3$ and CeO$_2$ phases and a more modulated basicity. Finally, this fact favours the transfer of dissociated H to hydrogenate near-adsorbed CO$_2$ at the studied operating temperature. As a result, the material obtained after the reduction of the 30% LaNiO$_3$/CeO$_2$ formulation exhibits the highest CH$_4$ production, if the whole temperature range is considered. Specifically, its maximum CH$_4$ production per cycle is 104 μmol g^{-1} (440 °C) and its selectivity towards CH$_4$ formation is above 90% in the whole temperature range. Furthermore, this DFM also emerges as promising approach to promote the joint optimization of H$_2$ conversion and CH$_4$ production, since its present quite fast kinetics during CO$_2$ hydrogenation to methane.

The 30% LaNiO$_3$/CeO$_2$-derived DFM also shows promising properties for the real-world applicability. On the one hand, it demonstrates high stability during long-terms experiments under hard reactions conditions, even above than other conventional Ni-based DFMs. On the other hand, although, the presence of O$_2$ during the CO$_2$ capture step has a detrimental effect on CH$_4$ production, the decrease is lower than that reported for other conventional Ni-based catalysts. Indeed, the activity recovery capacity is higher when the system comes back to an oxygen-free environment due to the enhanced redox properties of this novel DFM. Thus, ceria-supported LaNiO$_3$ perovskites emerge as promising precursors of highly active, versatile and stable novel dual function materials for CO$_2$ adsorption and hydrogenation to methane under wide variety of operational conditions.

CRediT authorship contribution statement

Jon A. Onrubia-Calvo: Conceptualization, Methodology, Validation, Writing – original draft. **Alejandro Bermejo-López:** Methodology, Investigation. **Sonia Pérez-Vázquez:** Investigation. **Beñat Pereda-Ayo:** Conceptualization, Methodology, Visualization, Writing – review & editing. **José A. González-Marcos:** Methodology, Data curation, Supervision, Funding acquisition. **Juan R. González-Velasco:** Conceptualization, Supervision, Funding acquisition, Project administration.

Declaration of Competing Interest

The authors declare that they have no known competing financial interests or personal relationships that could have appeared to influence the work reported in this paper.

Acknowledgments

Appendix A. Supplementary data

Supporting information includes detailed information on characterization of fresh and used samples, i.e. Enlargement of XRD results, N_2 adsorption-desorption isotherms and CH_4 and CO_2 mass spectroscopy signals during H_2-TPR experiments. A comparison of CH_4 and CO productions with respect to conventional 10% Ni-15% CaO/Al_2O_3 during CO_2 adsorption and hydrogenation cycles is also included as reference. Supplementary data to this article can be found online at https://doi.org/10.1016/j.fuel.2022.123842.

References

[1] Wang S, Li G, Fang C. Urbanization, economic growth, energy consumption, and CO_2 emissions: Empirical evidence from countries with different income levels. Renew Sust Energ Rev 2018;81:2144–59. https://doi.org/10.1016/j.rser.2017.06.025.

[2] Abu-Saqer K, Lubbad SH. Assessment of various treatment methods and reagents for cleanup and conditioning of sphagnum peat moss as sorbents in removal of malachite green as a cationic organic dye probe from water. SN Appl Sci 2018;1(1):20. https://doi.org/10.1007/s42452-018-0021-z.

[3] Abirami B, Radhakrishnan M, Kumaran S, Wilson A. Impacts of global warming on marine microbial communities. Sci Total Environ 2021;791:147905. https://doi.org/10.1016/j.scitotenv.2021.147905.

[4] Porta A, Matarrese R, Visconti CG, Castoldi L, Lietti L. Storage material effects on the performance of Ru-based CO_2 capture and methanation dual functioning materials. Ind Eng Chem Res 2021;60(18):6706–18. https://doi.org/10.1021/acs.iecr.0c05898.

[5] Massol O, Tchung-Ming S, Banal-Estañol A. Capturing industrial CO_2 emissions in Spain: Infrastructures, costs and break-even prices. Energy Policy 2018;115:545–60. https://doi.org/10.1016/j.enpol.2018.01.015.

[6] Budinis S, Krevor S, Dowell NM, Brandon N, Hawkes A. An assessment of CCS costs, barriers and potential. Energy Strategy Rev 2018;22:61–81. https://doi.org/10.1016/j.esr.2018.08.003.

[7] Gao W, Liang S, Wang R, Jiang Q, Zhang Y, Zheng Q, et al. Industrial carbon dioxide capture and utilization: State of the art and future challenges. Chem Soc Rev 2020;49(23):8584–686. https://doi.org/10.1039/D0CS00025F.

[8] Duyar MS, Treviño MAA, Farrauto RJ. Dual function materials for CO_2 capture and conversion using renewable H_2. Appl Catal B 2015;168–169:370–6. https://doi.org/10.1016/j.apcatb.2014.12.025.

[9] Duyar M, Farrauto R, Park A. Methods systems and materials for capturing carbon dioxide and converting it to a chemical product (U.S Patent No. WO/2016/007825). University of Columbia: New York, NY, USA. 14-01-2016.

[10] Ghaib K, Ben-Fares F. Power-to-methane: A state-of-the-art review. Renew Sust Energ Rev 2018;81:433–46. https://doi.org/10.1016/j.rser.2017.08.004.

[11] Bermejo-López A, Pereda-Ayo B, González-Marcos JA, González-Velasco JR. Alternate cycles of CO_2 storage and in situ hydrogenation to CH_4 on Ni–Na_2CO_3/Al_2O_3: Influence of promoter addition and calcination temperature. Sustain Energy Fuels 2021;5(4):1194–210. https://doi.org/10.1039/D0SE01677B. DOI: 10.1039/D0SE01677B.

[12] Sabatier P. New synthesis of methane. Comptes Rendus 1902;134:514–6. https://ci.nii.ac.jp/naid/20001066147/en/.

[13] Bermejo-López A, Pereda-Ayo B, González-Marcos JA, González-Velasco JR. Mechanism of the CO_2 storage and in situ hydrogenation to CH_4. temperature and adsorbent loading effects over Ru-CaO/Al_2O_3 and Ru-Na_2CO_3/Al_2O_3 catalysts. Appl Catal B 2019;256:117845.

[14] Cimino S, Boccia F, Lisi L. Effect of alkali promoters (li, na, K) on the performance of Ru/Al_2O_3 catalysts for CO_2 capture and hydrogenation to methane. J CO_2 Util 2020;37:195–203. https://doi.org/10.1016/j.jcou.2019.12.010.

[15] Bermejo-López A, Pereda-Ayo B, González-Marcos JA, González-Velasco JR. Ni loading effects on dual function materials for capture and in-situ conversion of CO_2 to CH_4 using CaO or Na_2CO_3. J CO_2 Util 2019;34:576–87. https://doi.org/10.1016/j.jcou.2019.08.011.

[16] Zhou Z, Sun N, Wang B, Han Z, Cao S, Hu D, et al. 2D-layered Ni–MgO–Al_2O_3 nanosheets for integrated capture and methanation of CO_2. ChemSusChem 2020;13(2):360–8. https://doi.org/10.1002/cssc.201902828.

[17] Kosaka F, Liu Y, Chen S, Mochizuki T, Takagi H, Urakawa A, et al. Enhanced activity of integrated CO_2 capture and reduction to CH_4 under pressurized conditions toward atmospheric CO_2 utilization. ACS Sustain Chem Eng 2021;9(9):3452–63. https://doi.org/10.1021/acssuschemeng.0c07162.

[18] Cimino S, Russo R, Lisi L. Insights into the cyclic CO_2 capture and catalytic methanation over highly performing Li-Ru/Al_2O_3 dual function materials. Chem Eng J 2022;428:131275. https://doi.org/10.1016/j.cej.2021.131275.

[19] Arellano-Treviño MA, He Z, Libby MC, Farrauto RJ. Catalysts and adsorbents for CO_2 capture and conversion with dual function materials: Limitations of ni-containing DFMs for flue gas applications. J CO_2 Util 2019;31:143–51. https://doi.org/10.1016/j.jcou.2019.03.009.

[20] Sun S, Sun H, Williams PT, Wu C. Recent advances in integrated CO_2 capture and utilization: A review. Sustain Energy Fuels 2021;5(18):4546–59. https://doi.org/10.1039/D1SE00797A.

[21] Hu Y, Guo Y, Sun J, Li H, Liu W. Progress in MgO sorbents for cyclic CO_2 capture: A comprehensive review. J Mater Chem A 2019;7(35):20103–20. https://doi.org/10.1039/C9TA06930E.

[22] Duyar MS, Ramachandran A, Wang C, Farrauto RJ. Kinetics of CO_2 methanation over Ru/γ-Al_2O_3 and implications for renewable energy storage applications. J CO_2 Util 2015;12:27–33. https://doi.org/10.1016/j.jcou.2015.10.003.

[23] Wang S, Schrunk ET, Mahajan H, Farrauto ARJ. The role of ruthenium in CO_2 capture and catalytic conversion to fuel by dual function materials (DFM). Catalysts 2017;7(3):88. https://doi.org/10.3390/catal7030088.

[24] Duyar MS, Wang S, Arellano-Treviño MA, Farrauto RJ. CO_2 utilization with a novel dual function material (DFM) for capture and catalytic conversion to synthetic natural gas: An update. J CO_2 Util 2016;15:65–71. https://doi.org/10.1016/j.jcou.2016.05.003.

[25] Porta A, Visconti CG, Castoldi L, Matarrese R, Jeong-Potter C, Farrauto RJ, et al. Ru-Ba synergistic effect in dual functioning materials for cyclic CO_2 capture and methanation. Appl Catal B 2021;283:119654. https://doi.org/10.1016/j.apcatb.2020.119654.

[26] Dai L, Lu X, Chu G, He C, Zhan W, Zhou G. Surface tuning of $LaCoO_3$ perovskite by acid etching to enhance its catalytic performance. Rare Met 2020;40:555–62. https://doi.org/10.1007/s12598-019-01360-w.

[27] Aziz MAA, Jalil AA, Triwahyono S, Ahmad A. CO_2 methanation over heterogeneous catalysts: Recent progress and future prospects. Green Chem 2015;17(15):2647–63. https://doi.org/10.1039/C5GC00119F.

[28] Ye RP, Li Q, Gong W, Wang T, Razink JJ, Lin L, et al. High-performance of nanostructured Ni/CeO_2 catalyst on CO_2 methanation. Appl Catal B 2020;268:118474. https://doi.org/10.1016/j.apcatb.2019.118474.

[29] Ye L, Ramirez Reina T, Liu J, Chevella D, Jin Y, Fan M, et al. Engineering Ni/SiO_2 catalysts for enhanced CO_2 methanation. Fuel 2021;285:119151. https://doi.org/10.1016/j.fuel.2020.119151.

[30] Nishihata Y, Mizuki J, Akao T, Tanaka H, Uenishi M, Kimura M, et al. Self-regeneration of a Pd-perovskite catalyst for automotive emissions control. Nature 2002;418(6894):164–7.

[31] Maneerung T, Hidajat K, Kawi S. K-doped $LaNiO_3$ perovskite for high-temperature water-gas shift of reformate gas: Role of potassium on suppressing methanation. Int J Hydrog Energy 2017;42(15):9840–57.

[32] Yang E-, Kim NY, Choi G, Lim SS, Moon DJ. Steam CO_2 reforming of methane over $La_{1-x}Ce_xNiO_3$ perovskite catalysts. 20th World Hydrogen Energy Conference, WHEC 2014. 2014;3:1618-1626. Accessed 26 September 2019. http://pubs.kist.re.kr/handle/201004/48729.

[33] Gao J, Jia L, Fang W, Li Q, Song H. Methanation of carbon dioxide over the $LaNiO_3$ perovskite catalysts activated under the reactant stream. Fuel. Chem Technol 2009;37(5):573–7. https://doi.org/10.1016/S1872-5813(10)60008-4.

[34] Li S, Guo S, Gong D, Kang N, Fang K, Liu Y. Nano composite composed of MoO_x-La_2O_3Ni on SiO_2 for storing hydrogen into CH_4 via CO_2 methanation. Int J Hydrog Energy 2019;44(3):1597–609. https://doi.org/10.1016/j.ijhydene.2018.11.130.

[35] Wang X, Zhu L, Zhuo Y, Zhu Y, Wang S. Enhancement of CO_2 Methanation over La-Modified Ni/SBA-15 Catalysts Prepared by Different Doping Methods ACS Sustainable Chem. Eng 2019;7:14647–60. https://doi.org/10.1021/acssuschemeng.9b02563.

[36] Aldana PAU, Ocampo F, Kobl K, Louis B, Thibault-Starzyk F, Daturi M, et al. Catalytic CO_2 valorization into CH_4 on Ni-based ceria-zirconia. reaction mechanism by operando IR spectroscopy. Catal Today 2013;215:201–7. https://doi.org/10.1016/j.cattod.2013.02.019.

[37] Tada S, Shimizu T, Kameyama H, Haneda T, Kikuchi R. Ni/CeO_2 catalysts with high CO_2 methanation activity and high CH_4 selectivity at low temperatures. Int J Hydrog Energy 2012;37(7):5527–31. https://doi.org/10.1016/j.ijhydene.2011.12.122.

[38] Pan Q, Peng J, Sun T, Wang S, Wang S. Insight into the reaction route of CO_2 methanation: Promotion effect of medium basic sites. Catal Commun 2014;45:74–8. https://doi.org/10.1016/j.catcom.2013.10.034.

[39] Onrubia-Calvo J, Pereda-Ayo B, González-Marcos JA, Bueno-López A, González-Velasco JR. Design of CeO_2-supported $LaNiO_3$ perovskites as precursors of highly active catalysts for CO_2 methanation. Catal Sci Technol 2021;11:6065–79. https://doi.org/10.1039/D1CY00659B.

[40] Gallego J, Sierra-Gallego G, Tapia J, Mondragón F, Batiot-Dupeyrat C. Activation of CO_2 on Ni/La_2O_3: Non-isothermal kinetic study on the basis of thermogravimetric studies. React Kinet Mech Catal 2016;119(1):179–93. https://doi.org/10.1007/s11144-016-1032-7.

[41] Bakiz B, Guinneton F, Arab M, Benlhachemi A, Villain S, Satre P, et al. Carbonatation and decarbonatation kinetics in the La_2O_3-$La_2O_2CO_3$ system under CO_2 gas flows. Adv Mater Sci 2010;2010:1–6.

[42] Cárdenas-Arenas A, Quindimil A, Davó-Quiñonero A, Bailón-García E, Lozano-Castelló D, De-La-Torre U, et al. Design of active sites in Ni/CeO_2 catalysts for the methanation of CO_2: Tailoring the Ni-CeO_2 contact. Appl Mater Today 2020;19:100591. https://doi.org/10.1016/j.apmt.2020.100591.

[43] Quindimil A, De-La-Torre U, Pereda-Ayo B, Davó-Quiñonero A, Bailón-García E, Lozano-Castelló D, et al. Effect of metal loading on the CO_2 methanation: A comparison between alumina supported Ni and Ru catalysts. Catal Today 2019;356:419–32. https://doi.org/10.1016/j.cattod.2019.06.027.

[44] Li S, Liu G, Zhang S, An K, Ma Z, Wang L, et al. Cerium-modified Ni-La_2O_3/ZrO_2 for CO_2 methanation. J Energy Chem 2020;43:155–64. https://doi.org/10.1016/j.jechem.2019.08.024.

[45] Iglesias I, Quindimil A, Mariño F, De-La-Torre U, González-Velasco JR. Zr promotion effect in CO_2 methanation over ceria supported nickel catalysts. Int J Hydrog Energy 2019;44(3):1710–9. https://doi.org/10.1016/j.ijhydene.2018.11.059.

[46] Atzori L, Cutrufello MG, Meloni D, Monaci R, Cannas C, Gazzoli D, et al. CO_2 methanation on hard-templated NiO-CeO$_2$ mixed oxides. Int J Hydrog Energy 2017;42(32):20689–702. https://doi.org/10.1016/j.ijhydene.2017.06.198.

[47] Kwak JH, Kovarik L, Szanyi J. Heterogeneous catalysis on atomically dispersed supported metals: CO_2 reduction on multifunctional Pd catalysts. ACS Catal 2013;3 (9):2094–100. https://doi.org/10.1021/cs4001392. 10.1021/cs4001392.

[48] Yu Y, Bian Z, Song F, Wang J, Zhong Q, Kawi S. Influence of calcination temperature on activity and selectivity of Ni–CeO$_2$ and Ni–Ce$_{0.8}$Zr$_{0.2}$O$_2$ catalysts for CO_2 methanation. Top Catal 2018;61(15):1514–27. https://doi.org/10.1007/s11244-018-1010-6.

[49] Cárdenas-Arenas A, Quindimil A, Davó-Quiñonero A, Bailón-García E, Lozano-Castelló D, De-La-Torre U, et al. Isotopic and in situ DRIFTS study of the CO_2 methanation mechanism using Ni/CeO$_2$ and Ni/Al$_2$O$_3$ catalysts. Appl Catal B 2020; 265:118538. https://doi.org/10.1016/j.apcatb.2019.118538.

[50] Le TA, Kim TW, Lee SH, Park ED. Effects of Na content in Na/Ni/SiO$_2$ and Na/Ni/CeO$_2$ catalysts for CO and CO_2 methanation. Catal Today 2018;303:159–67. https://doi.org/10.1016/j.cattod.2017.09.031.

[51] Xu L, Yang H, Chen M, Wang F, Nie D, Qi L, et al. CO_2 methanation over ca doped ordered mesoporous Ni-Al composite oxide catalysts: The promoting effect of basic modifier. J CO_2 Util 2017;21:200–10. https://doi.org/10.1016/j.jcou.2017.07.014.

[52] Bermejo-López A, Pereda-Ayo B, González-Marcos JA, González-Velasco JR. Simulation-based optimization of cycle timing for CO_2 capture and hydrogenation with dual function catalyst. Catal Today 2021. https://doi.org/10.1016/j.cattod.2021.08.023.

[53] Bermejo-López A, Pereda-Ayo B, González-Marcos JA, González-Velasco JR. Modeling the CO_2 capture and in situ conversion to CH$_4$ on dual function Ru-Na$_2$CO$_3$/Al$_2$O$_3$ catalyst. J CO_2 Util 2020;42:101351.

[54] Zheng Q, Farrauto R, Chau NA. Adsorption and methanation of flue gas CO_2 with dual functional catalytic materials: A parametric study. Ind Eng Chem Res 2016;55 (24):6768–76. https://doi.org/10.1021/acs.iecr.6b01275.

[55] Mutz B, Carvalho HWP, Mangold S, Kleist W, Grunwaldt J. Methanation of CO_2: Structural response of a ni-based catalyst under fluctuating reaction conditions unraveled by operando spectroscopy. J Catal 2015;327:48–53. https://doi.org/10.1016/j.jcat.2015.04.006.

[56] Mutz B, Gänzler AM, Nachtegaal M, Müller O, Frahm R, Kleist W, et al. Surface oxidation of supported Ni particles and its impact on the catalytic performance during dynamically operated methanation of CO_2. Catalysts 2017;7(9):279. https://doi.org/10.3390/catal7090279.